J. Fluid Mech. (2024), *vol*. 985, A31, doi:10.1017/jfm.2024.307

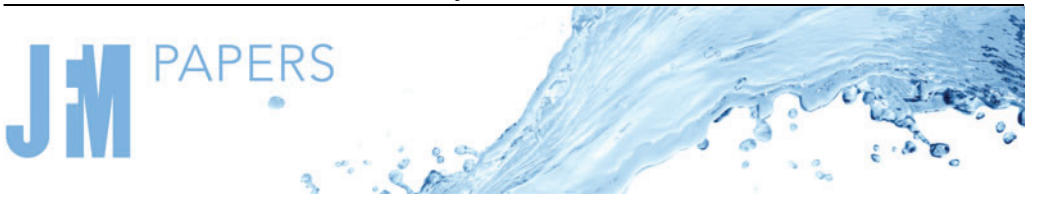

Experiments on symmetry breaking of azimuthal combustion instabilities and their analysis combining acoustic energy balance and flame describing functions

V. Latour[1],†, **D. Durox**[1], **A. Renaud**[1] **and S. Candel**[1]

[1]Laboratoire EM2C, CNRS, CentraleSupélec, Université Paris-Saclay, 3, rue Joliot Curie, 91192 Gif-sur-Yvette CEDEX, France

(Received 19 July 2023; revised 31 January 2024; accepted 21 March 2024)

Combustion instabilities in annular systems raise fundamental issues that are also of practical importance to aircraft engines and ground-based gas turbine combustors. Recent studies indicate that the injector plays a significant role in the stability of combustors by defining the flame dynamical response and setting the inlet impedance of the system. The present investigation examines the effects of combinations of injectors of two different types (*U* and *S*) on thermoacoustic instabilities in a laboratory-scale annular combustor and compares different circumferential staging strategies. The combustor operates in a stable fashion when all injection units belong to the *S*-family, but exhibits large amplitude pressure oscillations when all these units are of the *U*-type. When the system comprises a mix of *U*- and *S*-injectors, it is possible to determine the number of *S*-injectors leading to stable operation. For a fixed proportion of *U*- and *S*-injectors, some arrangements give rise to stable operation while others do not. Results also show that introducing symmetry-breaking elements affects the system's modal dynamics. These experimental observations are interpreted in an acoustic energy balance framework used to derive an expression for the growth rate as a function of the describing functions of the flames formed by the different injectors and their respective azimuthal locations. Growth rates are determined for the different configurations and used to explain the various observations, estimate the system damping rate and predict the location of the nodal line when the standing mode prevails.

Key words: combustion, acoustics

† Email address for correspondence: veranika.latour@centralesupelec.fr

1. Introduction

Thermoacoustic instabilities result from a constructive coupling between the acoustics of the system and the combustion process. On the fundamental level, these phenomena raise many scientific issues concerning the driving processes, the coupling mechanisms and their reduced-order modelling. In practice, these instabilities give rise to large amplitude pressure oscillations that sometimes reach levels of a few percent of the mean chamber pressure, producing intense heat release rate fluctuations in the combustion system, and submitting its structure and components to enhanced vibrations and thermal loads. These phenomena can lead to cyclic fatigue and cause severe damage to the combustion chamber, eventually leading to the mechanical failure of the system (Candel 2002; Huang & Yang 2009; Poinsot 2017).

Much of the research effort in this field is currently focused on instabilities in high-performance devices and, in particular, in gas turbine combustors. These devices are, in most cases, annular, and in this geometry, instabilities can be coupled by axial and azimuthal modes. The azimuthal modes are generally considered to be the most dangerous because they are less well damped and their eigenfrequencies, determined by the perimeter of the chamber (which is the largest dimension of the system), lie in the low-frequency range where the flames are most susceptible to disturbances. An intensive research effort has been carried out through theoretical analysis (Evesque & Polifke 2002; Parmentier *et al.* 2012; Ghirardo & Juniper 2013; Noiray & Schuermans 2013; Campa & Camporeale 2014; Bothien, Noiray & Schuermans 2015), experiments (Krebs *et al.* 2002; Kopitz *et al.* 2005; Fanaca *et al.* 2008; Bourgouin *et al.* 2013; Worth & Dawson 2013; Prieur *et al.* 2017; Indlekofer *et al.* 2021; Rajendram Soundararajan *et al.* 2021) and numerical simulations (Pankiewitz & Sattelmayer 2003; Staffelbach *et al.* 2009; Wolf *et al.* 2012) to better understand the physical phenomena at stake and more reliably predict thermoacoustic oscillations at an early stage of the combustor design process.

The present article aims to provide further insights into the coupling giving rise to azimuthal instabilities in annular combustors. This is achieved by making use of systematic experimentation. The central idea is to use two families of injection units that give rise to flames with notably different dynamical characteristics, and consider various combinations of these units to examine the dynamics of the annular combustor, the transition between unstable and stable operation, analyse the modal structure that couples self-sustained oscillations and identify implications in terms of symmetry breaking. A second objective of this article is to propose an interpretation of these data using an analytical framework combining acoustic energy balance principles and measured flame describing functions.

Since the present article investigates symmetry breaking induced by mixing different types of injection units, it is natural to stress their role in combustion instabilities arising in swirl-stabilized combustors. First, these units influence the acoustics of the system through the impedance they impose at the inlet of the combustion chamber (Fischer, Hirsch & Sattelmayer 2006; Huang & Yang 2009; Rajendram Soundararajan *et al.* 2022*b*). Second, the injection system determines the swirl number, flow pattern, spray geometry and droplet size distribution, which essentially define the flame structure, the heat release rate distribution and consequently the flame dynamics, i.e. the flame's response to acoustic disturbances that is commonly characterized by flame describing functions. Large eddy simulations carried out by Huang & Yang (2005) reveal the effect of inlet swirl on flow pattern and combustion dynamics. Experiments indicate that flame dynamics is notably influenced by the axial position of the swirl generator (Komarek & Polifke 2010)

and the injection unit pressure drop and swirl number (Vignat *et al.* 2019; Rajendram Soundararajan *et al.* 2022*a*).

Annular combustors feature a rotational symmetry when identical injection units are regularly spaced around the circumference of the annulus. Symmetry breaking and staging concepts (introduction of asymmetry in the annular system by mixing injectors presenting different characteristics) have been the subject of theoretical, numerical and experimental investigations to assess the suitability of these strategies to reduce and control thermoacoustic instabilities coupled by azimuthal modes.

Noiray, Bothien & Schuermans (2011) examined circumferential staging by testing configurations mixing two types of burners using a theoretical framework and thermoacoustic network simulations. Analytical expressions derived from dynamic system theory enable to identify a bifurcation parameter, which, in the case of an unstable nth azimuthal mode, is the $2n$ component of the Fourier expansion of the azimuthal distribution of flame transfer functions. The value of this parameter defines the nature of the unstable mode encountered in the annular configuration: standing, spinning or mixed. The analysis is pursued by Ghirardo & Juniper (2013) to include effects of transverse excitation of the flames and by Bothien *et al.* (2015) who consider the circumferential staging effect due to different flame responses. Parmentier *et al.* (2012) developed an analytical model and investigated symmetry breaking in the case of an annular system with four burners, where two types of burners are mixed. It was shown in that study that passive control of azimuthal instabilities is more effective when burners of the same type are located side by side and not when they are orientated symmetrically. Bauerheim *et al.* (2014) extended this analytical approach to an annular system with N identical or non-identical burners. Two parameters affecting the stability of the system were highlighted: the coupling strength, corresponding to the cumulative effects of the N flames, which controls the stability at first order; and the splitting strength, resulting from symmetry breaking when the flames are different, which affects the nature of the mode. The model also shows that mixing two types of injectors promotes non-degenerate modes and favours the occurrence of standing modes. More recent additions to the literature pursue the theoretical analysis of symmetry breaking using uncertainty quantification (Bauerheim *et al.* 2016) or the adjoint perturbation framework (Mensah *et al.* 2019).

On the experimental level, the effects of asymmetric power distribution in an annular Rijke tube arrangement were investigated by Moeck, Paul & Paschereit (2010) through azimuthal variations of the electrical power supplied to each heating grid. Different unstable modes are found and the influence of heating distribution on the damping of instabilities is analysed. More recently, Humbert *et al.* (2023) examined the effects of symmetry breaking on the degeneracy and nature of azimuthal thermoacoustic modes of an annular combustor model with electroacoustic feedback. Aguilar *et al.* (2021) showed the effects of symmetry breaking on the location of the pressure anti-nodal line in the MICCA annular chamber equipped with laminar matrix burners. Symmetry breaking was achieved by partially blocking the holes of some matrix burners. It was found that if the expected oscillation for the operating point in the symmetrical situation is a standing mode, the introduction of symmetry breaking favours this mode type and the position of the nodal line locks in the region where the symmetry breaking elements are located. When the expected mode in the symmetrical configuration is of the spinning type, symmetry breaking does not lead to the appearance of a standing mode, indicating, according to the authors, that the symmetry breaking had to be stronger to change the nature of the mode. The effects of symmetry breaking on the modes in annular combustors and nodal line locking are discussed further in § 3.3.

In addition to 'geometrical symmetry breaking' (mixing injectors with different characteristics), Bauerheim, Cazalens & Poinsot (2015) analysed the case of 'flow symmetry breaking', resulting from a mean swirling motion in the annular system, which splits azimuthal modes into two waves having unequal but close frequencies and structures. Compared with the degenerate modes prevailing in the absence of mean azimuthal flow, the spinning mode is favoured. Humbert *et al.* (2021) imposed a mean tangential flow in an annular system equipped with electroacoustic actuators and observed the formation of beats due to the degeneracy loss of the acoustic mode, resulting from the small frequency difference between the clockwise and counterclockwise travelling waves.

Introducing Helmholtz resonators or baffles in an annular system constitutes another means of symmetry breaking. An analytical investigation of the best placement of Helmholtz resonators for the damping of azimuthal instabilities in an annular system can be found from Stow & Dowling (2003), and the authors showed that Helmholtz resonators introduce circumferential mode coupling. The damping effect of baffles number and position on thermoacoustic instabilities in an annular combustor was experimentally studied by Dawson & Worth (2015). The authors report that even if no damping was observed with a single baffle, the azimuthal symmetry is broken, leading to a coupling between the counterclockwise (CCW) and clockwise (CW) azimuthal waves, promoting a standing mode.

The present article proposes to investigate circumferential staging by examining configurations mixing two types of injection units that were recently found to belong to distinct categories with different flame dynamics, namely low-swirl moderate-pressure drop and high-swirl high-pressure drop units (Rajendram Soundararajan *et al.* 2022*a*). Injectors of the former category (denoted '707' in the last reference but referred to as '*S*-injectors' in what follows) were found to lead to stable operation in MICCA-Spray, whereas others ('*U*-injectors', denoted '727' in the last reference) led to unstable oscillations over a relatively broad operating domain (thermal power from 93 to 118 kW and global equivalence ratio between 0.75 and 1.05). In the same range of operation, different arrangements of *U*- and *S*-injectors are examined in the present study and the experimental results are interpreted using an analytical framework derived from acoustic energy balance equations and used to evaluate the growth rate. The key idea is to identify the contribution of the different flames to the global energy source term of the system by making use of an analytical expression of the source term depending on the injection units' azimuthal location in the system and on flame describing functions, here experimentally determined in a single-sector configuration, designated as SICCA-Spray.

After a presentation of the annular combustor MICCA-Spray and the injectors' characteristics (§ 2), different arrangements of *U*- and *S*-injectors are tested (§ 3). Systematic experiments indicate that the number of *S*-injectors changes the level of pressure fluctuations in the system and, for a given number of *S*-injectors in the system, their relative position also has a notable influence, not only on the level of pressure fluctuations, but also on modal dynamics and the nodal line location. A theoretical framework based on acoustic energy balance equations and flame describing functions is derived in § 4 to interpret the experimental observations through the determination of the growth rates for the different configurations and estimate the damping rate in the annular system.

2. Experimental set-up, injectors' characteristics and modal identification

The MICCA-Spray annular combustor is first presented. Then, the characteristics of the two types of injector used in this study are compared, based on their flame describing

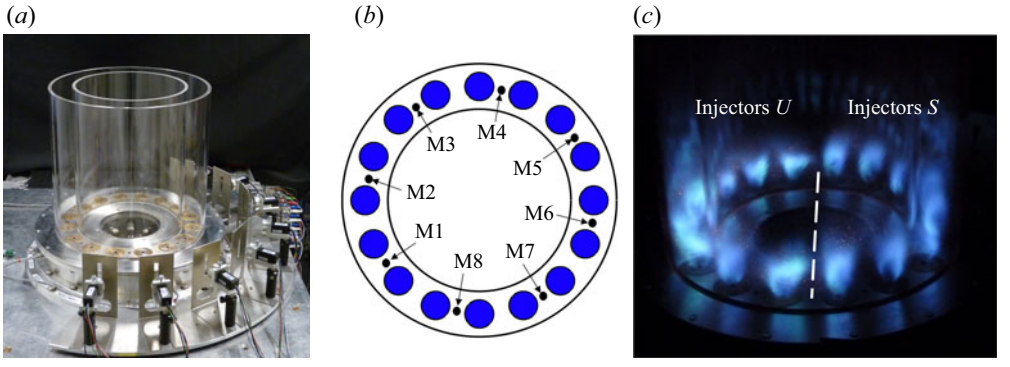

Figure 1. (*a*) MICCA-Spray test rig and array of the eight photomultipliers used to measure OH* emission from the flames (these sensors are employed in § 4.2 and Appendix C). (*b*) Top view of MICCA-Spray and microphones positions. (*c*) MICCA-Spray equipped with eight *U*-injectors placed on one half of the annulus and eight *S*-injectors on the other half. The white dashed line separates *U* and *S* injection units.

functions, measured in the single-sector configuration, SICCA-Spray. Finally, §§ 2.3 and 2.4 describe the acoustic mode structures that can be observed in annular systems and the modal identification procedure.

2.1. *The MICCA-spray annular system*

The MICCA-spray annular combustion chamber, shown in figure 1, is formed by two quartz walls of the same length, $l = 400$ mm, of outer diameter 300 mm for the inner cylinder and inner diameter 400 mm for the outer quartz cylinder. The backplane comprises 16 regularly spaced injection units, which deliver liquid fuel, heptane in the present experiments, as a hollow cone spray of droplets mixed with air (Vignat *et al.* 2021). The air mass flow rate is controlled through two Bronkhorst EL-FLOW mass flow meters and the fuel mass flow rate through a Bronkhorst CORI-FLOW mass flow rate controller. Eight Brüel & Kjær microphones, flush-mounted on waveguides to protect them from the hot gas temperature environment, enable to record pressure fluctuations at the combustion chamber backplane, with a sampling frequency $f_s = 32\,768$ Hz.

The stability maps of MICCA-Spray equipped with these two types of injectors are presented by Rajendram Soundararajan *et al.* (2022*a*). In that reference, as already mentioned, 'injector *S*' is denoted '707' and 'injector *U*', '727'. The operating point chosen for the present study corresponds to a thermal power value $\mathcal{P} = 118$ kW and a global equivalence ratio $\phi = 0.9$. Under these conditions, the chamber is unstable when it is equipped with *U*-injectors and stable when it is equipped with *S*-injectors.

2.2. *Injectors' characteristics and flame describing functions*

An exploded view of the injection units used in this study is presented in figure 2(*c*). These injectors are composed of four main elements: an air distributor, a liquid fuel atomizer, a swirler and a terminal plate with a convergent nozzle. Changing the swirler changes the swirl number and pressure drop through the injection unit.

The characteristics of injectors *U* and *S* (swirl number, pressure drop and pressure drop coefficient) are gathered in table 1. Injector *S* presents a lower swirl number and a lower pressure drop value than injector *U*.

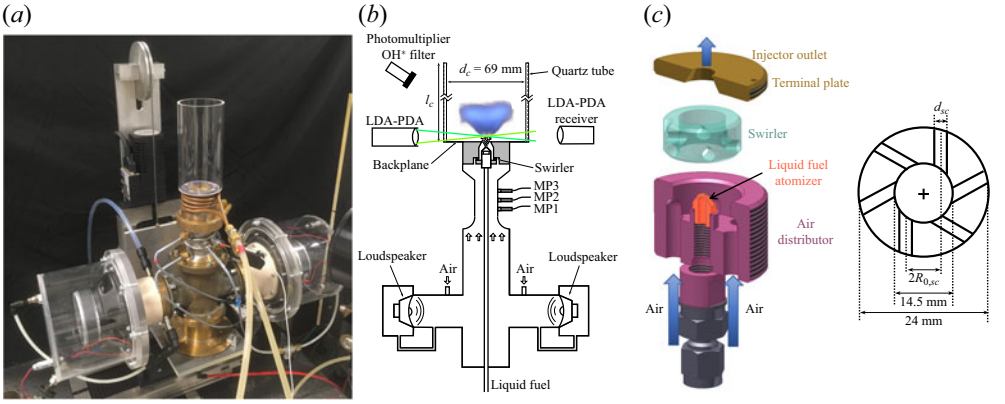

Figure 2. (*a*) SICCA-Spray set-up, (*b*) SICCA-Spray configuration for FDF measurements and (*c*) exploded view of the injector along with a top view of the swirler.

Injector	S_N	Δp (kPa)	σ
Injector *S* (stable in MICCA-Spray)	0.60	3.65	3.33
Injector *U* (unstable in MICCA-Spray)	0.74	5.70	5.20

Table 1. Injectors' characteristics: swirl number (S_N), pressure drop (Δp) and pressure drop coefficient (σ), obtained from measurements under cold conditions for an air mass flow rate of 2.3 g s^{-1} (Vignat *et al.* 2021).

It is also interesting to examine the effects of the injector characteristics on flame dynamics through the measurement of flame describing functions (FDFs). FDFs characterize the response of flames to acoustic disturbances and the FDF framework (Dowling 1997; Noiray *et al.* 2008), which is the nonlinear extension of flame transfer functions, is now widely used in combustion system stability analysis. They enable to capture saturation effects on the flame response and explain nonlinear phenomena such as triggering, mode hopping or hysteresis. FDFs are the subject of theoretical investigations (Ghirardo *et al.* 2015; Orchini, Illingworth & Juniper 2015) and are commonly used as an input in reduced-order models to interpret experimental observations (Schuermans *et al.* 2010; Paliès *et al.* 2011; Han, Li & Morgans 2015; Schuller, Poinsot & Candel 2020).

FDF measurements are carried out in a single-injector configuration, SICCA-Spray, displayed in figure 2, representing one sector of the annular system MICCA-Spray. The system can be modulated from the upstream side of the injector by two driver units placed at the bottom of the plenum and connected to a sinewave generator. The operating point in SICCA-Spray is chosen so that it corresponds to the thermal power value of one injector in MICCA-Spray, that is to say, 1/16th of the total thermal power in MICCA-Spray.

With the type of injectors used, equivalence ratio fluctuations are small compared with velocity fluctuations, so that the flame behaves in a quasi-premixed fashion (Rajendram Soundararajan *et al.* 2022*b*). FDFs are thus defined as the ratio of relative heat release rate fluctuations to relative volume flow rate fluctuations

$$\mathcal{F}(f, q') = \frac{\dot{Q}'/\bar{\dot{Q}}}{q'/\bar{q}} = G(f, q') \exp(\mathrm{i}\varphi(f, q')). \tag{2.1}$$

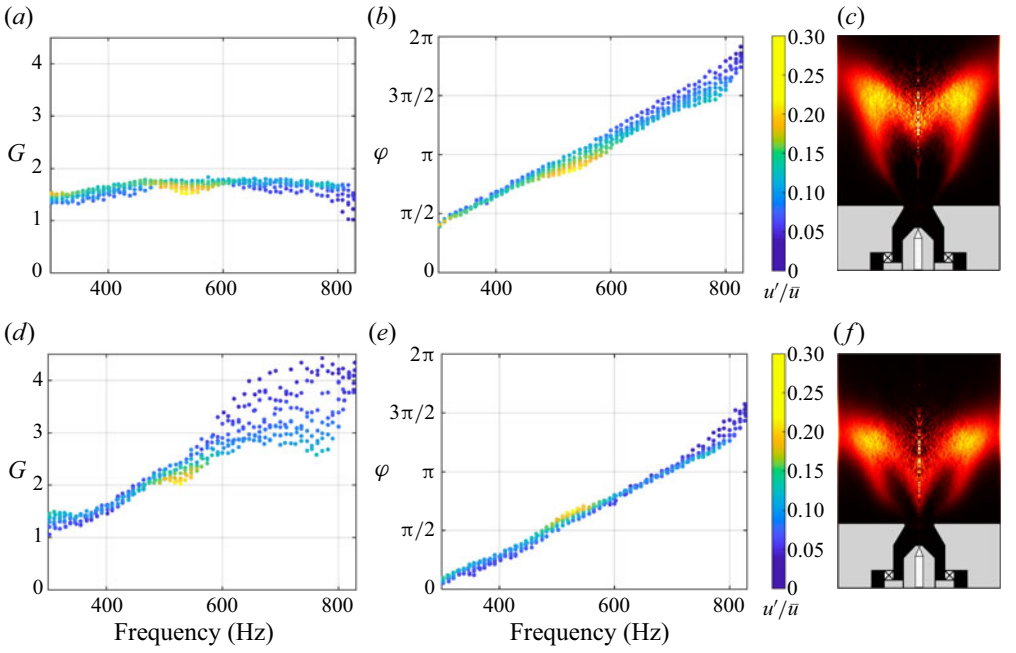

Figure 3. (*a*,*d*) Flame describing function gain, (*b*,*e*) flame describing function phase, and (*c*,*f*) OH* chemiluminescence distributions obtained after Abel inversion of the average images recorded by an intensified CCD camera, under stable operation in SICCA-Spray: (*a–c*) *S*-injector, (*d–f*) *U*-injector.

Relative heat release rate fluctuations are measured with a photomultiplier equipped with an OH* filter centred at 310 nm. The injector being weakly transparent to acoustic waves, relative velocity fluctuations measured upstream of the injector are not the same as those measured on its downstream side. Hence, velocity fluctuations are measured with a laser Doppler anemometry system (Dantec Dynamics), in the combustion chamber, at a position ($z = 2.5$ mm above the backplane and at $r = 3.5$ mm from the centre for injector *S* and at $r = 4.0$ mm for injector *U*) where relative velocity fluctuations match relative volume flow rate fluctuations, to comply with the FDF definition (Rajendram Soundararajan *et al.* 2022*b*). The fuel droplets, featuring a mean diameter below 5 μm at the measurement positions, can serve as flow tracers in the frequency range of interest (250–850 Hz). Measurements are carried out for seven levels of modulation amplitudes, corresponding to different voltage outputs of the sinewave generator, and leading to different values of relative velocity fluctuations depending on the frequency and the level of the modulation amplitude.

FDFs measured in SICCA-Spray equipped with injectors *U* and *S* are displayed in figure 3. FDF gain values are substantially lower for injector *S* than for injector *U*, and this is particularly true in a range of frequencies around 800 Hz, close to the eigenfrequency of the 1A1L (1st azimuthal–1st longitudinal) mode of the MICCA-Spray annular combustion chamber, involved in the combustion/acoustics coupling, as will be detailed in the next section. Differences in phases are also observed, with higher phase values for injector *S* than injector *U* in the range of frequencies investigated. Figure 3 also displays flame images obtained from the Abel inversion of the images captured with a charge-coupled device (CCD) camera, to show the effect of the injector pressure drop and swirl number on the flame shape. The '*V*' shaped flame obtained with injector *S* is longer and narrower

than that obtained with injector U, a hollow 'M' shape flame which is more compact, due to a higher swirl number of the injection unit.

Another effect that deserves to be considered is that injectors U and S have different pressure drop coefficients. When these injectors are mixed in various proportions, the air flow velocities through these units will not be the same, and since the mass flow rate of fuel is unaffected, the equivalence ratios will also differ for the two types of injectors and their operating point will be shifted with respect to the case where all injection units are the same. Calculations reported in Appendix A indicate that the operating point for U-injectors are shifted towards higher equivalence ratio values, while those of S-injectors change towards lower values and that the changes depend on the number of U and S injectors. It is shown however in Appendix A, through FDF measurements for different equivalence ratio values, that the variations encountered in this study only have a slight effect on the FDF gain and phase values, and hence on the flame dynamics of the individual flames.

2.3. *Modal structures and frequencies*

At this point, it is worth briefly describing the acoustic mode structures that can be observed in annular systems, specify those that are effectively observed experimentally and obtain an estimate of the corresponding eigenfrequencies. In the present configuration, the annulus mean radius R is large compared with the width of the annulus, and one may neglect any radial variation. Then, the large ratio between the surface area of the backplane and that of the injector outlet induces a decoupling of the plenum and the combustion chamber: the combustion chamber modes are weakly influenced by the plenum acoustics, as shown by Schuller *et al.* (2012), where conditions on temperatures and area ratios to obtain decoupled cavities are discussed. Furthermore, the injectors used are weakly transparent to acoustic waves, accentuating the decoupling (Rajendram Soundararajan *et al.* 2022*b*; Latour *et al.* 2024). Hence, the chamber backplane acts like a rigid wall and the exhaust is open to the atmosphere. In this configuration, the acoustic coupling modes are of the mixed axial-azimuthal type and may be designated by mA, nL. The pressure field can be cast in the following form:

$$\tilde{p}_{mn}(x,\theta,t) = [A^{+}_{mn}\exp(\mathrm{i}m\theta - \mathrm{i}\omega_{mn}t) + A^{-}_{mn}\exp(-\mathrm{i}m\theta - \mathrm{i}\omega_{mn}t)]\psi_n(x). \tag{2.2}$$

In this expression, m and n are integers, with $m \geqslant 0$ and $n \geqslant 1$, θ is the azimuthal angle considered positive in the CCW direction, and ω_{mn} is the angular frequency. The amplitudes A^{+}_{mn} and A^{-}_{mn} correspond to CCW and CW spinning waves, respectively, and $\psi_n(x)$ is the axial wavefunction satisfying the boundary conditions on the chamber backplane and at its exhaust. In the present case, the backplane is rigid and the outlet is open to the atmosphere, i.e. corresponds to a pressure node (in fact, the pressure does not quite vanish at the outlet but at a short distance from that section, and this may be accommodated by adding an end correction δ_a to the length of the chamber and replacing this length by $l' = l + \delta_a$). The longitudinal eigenfunctions are, in this case: $\psi_n(x) = \cos[(2n-1)\pi x/(2l')]$. The eigenfrequencies corresponding to the previous modes are then given by a standard expression:

$$f_{mn} = \left[m^2 \left(\frac{c}{\mathcal{P}_a}\right)^2 + (2n-1)^2 \left(\frac{c}{4l'}\right)^2 \right]^{1/2}, \tag{2.3}$$

where $\mathcal{P}_a = 2\pi R$ is the mean perimeter of the system and c, the speed of sound. In all the present experiments, one observes the 1A1L mode corresponding to $m = 1$ and $n = 1$,

and one may simplify the notation by neglecting the indices m and n in the pressure field expression:

$$\tilde{p}(x, \theta, t) = [A^{+} \exp(\mathrm{i}\theta - \mathrm{i}\omega t) + A^{-} \exp(-\mathrm{i}\theta - \mathrm{i}\omega t)]\psi(x). \tag{2.4}$$

It is worth mentioning that this expression of the pressure field does not capture nearfield modifications associated with the flames. One may also think that the purely azimuthal structure will be perturbed by the different staging patterns. However, these effects are expected to be small and this is confirmed by experimental measurements of the annular distributions of pressure signals as will be seen later on. Thus, (2.4) constitutes a reasonable approximation of the pressure field.

Finally, the eigenfrequency of this mode writes

$$f_{11} = \left[\left(\frac{c}{\mathcal{P}_a} \right)^2 + \left(\frac{c}{4l'} \right)^2 \right]^{1/2}. \tag{2.5}$$

It is now worth estimating the resonant frequency using the last expression. In the MICCA-Spray experiments, the perimeter $\mathcal{P}_a \simeq 1.1$ m. The end correction for an annular system is not well known theoretically, but some pressure measurements near the chamber exhaust indicate that $\delta_a \simeq 0.09$ m so that $l' \simeq 0.49$ m. Assuming an average temperature in the chamber $T \simeq 1500$ K and defining a speed of sound $c = 761\ \mathrm{m\,s^{-1}}$, the eigenfrequency of the 1A1L mode is $f_{11} \simeq 808$ Hz. We will see that this value is close to the peak frequencies observed experimentally, indicating that the coupling mode is essentially defined in this set-up by the combustion chamber modes and that most oscillations are of the 1A1L type.

For more complex geometries (for example, in the case of a coupling between the plenum and the combustion chamber), the eigenfrequencies of the modes involved in the combustion/acoustics coupling can be found using a Helmholtz solver, where the geometry and temperatures in the various cavities can be specified (Bourgouin *et al.* 2013). It is important to stress that the presence of the flame acting as an unsteady heat release source modifies the resonant loop, possibly shifting the oscillation frequency of the system with respect to the modal eigenfrequency (Durox, Schuller & Candel 2002; Schuller *et al.* 2020). However, the acoustic method exposed previously provides a reasonable first approximation of the thermoacoustic oscillation frequency, which can then be refined with a perturbation/correction procedure.

2.4. *Modal identification*

The signals recorded by the eight waveguided microphones plugged on the chamber backplane can be used to determine the frequency of oscillation of the modes coupling the instability. The peak frequency is obtained from the power spectral density (PSD) of these microphone signals. The PSD is calculated using Welch's method applied to 63 blocks of 8192 samples with a 50 % overlap and a Hamming window weighting. With these parameters, the frequency resolution is $\Delta f = 4$ Hz. For all the unstable configurations investigated, the power spectral densities, which will be discussed further in § 4.3, only feature a main peak at the fundamental frequency. Cases leading to non-degenerate modes characterized by close eigenfrequencies, whose difference is below the resolution frequency, will also be examined.

The complex wave amplitudes A_{+} and A_{-} may be retrieved from the eight microphone signals by solving an overdetermined system of linear equations using a least squares

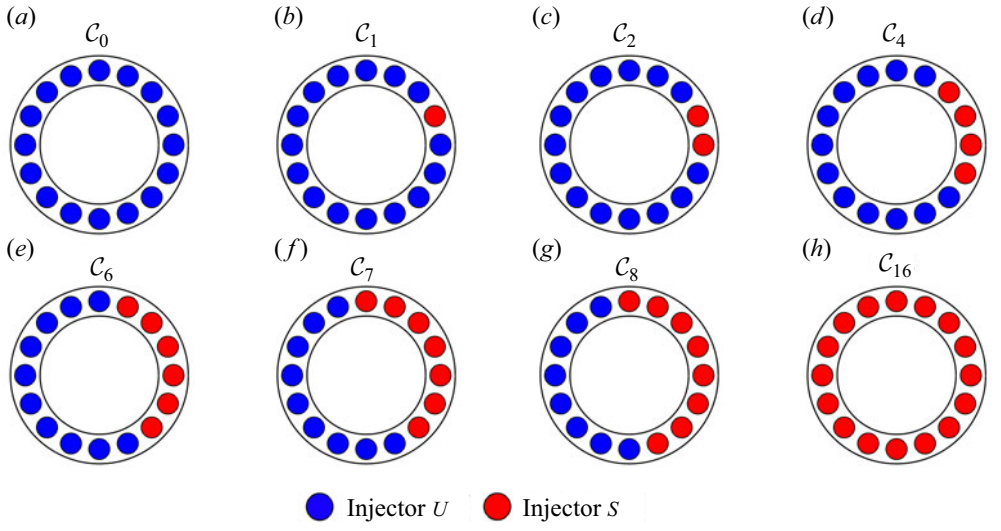

Figure 4. 'Side-by-side' (type $\mathcal{C}$) configurations investigated.

algorithm. One may then deduce the instability amplitude

$$A = [(A^+)^2 + (A^-)^2]^{1/2}, \tag{2.6}$$

which corresponds to a value averaged in time and space, and is independent of the instability mode.

3. Experimental results

Different arrangements of injectors U and S are now investigated. It is logical to begin with a configuration equipped with 16 U-injectors and then observe what happens when one successively introduces one to eight S-injectors in 'side-by-side' arrangements, where all the S-injectors are gathered on the same side of the annulus. One may then see how many U-injectors have to be replaced by S-injectors to completely dampen the instability. In a second step, the number of S-injectors is fixed and different positions for S-injectors are tested to examine how the relative position of S- and U-injectors impacts the level of pressure fluctuations in the system. In the last subsection, the effect of circumferential staging on the modal dynamics of the system is investigated.

3.1. *Side-by-side arrangements of S-injectors*

A first category of arrangements is investigated and will be referred to as '$\mathcal{C}$ arrangements'. Here, N_s S-injectors are placed side-to-side, with N_s ranging from 0, corresponding to the case where there are no S-injectors in the system, to $N_s = 8$, where half of the injectors is of the U type while the other half is of the S type. Pressure traces are also presented for a configuration comprising 16 S-injectors ($N_s = 16$) to complete the comparison. The eight investigated arrangements of this kind are displayed in figure 4.

Pressure time series for $N_s = 0$, 4, 8 and 16 are displayed in figure 5. When $N_s = 0$, the combustor exhibits high pressure fluctuation levels and when 16 S-injectors are mounted ($N_s = 16$), the system operates in a stable fashion. Replacing an increasing number of U-injectors by S-injectors diminishes the level of pressure fluctuations in the chamber.

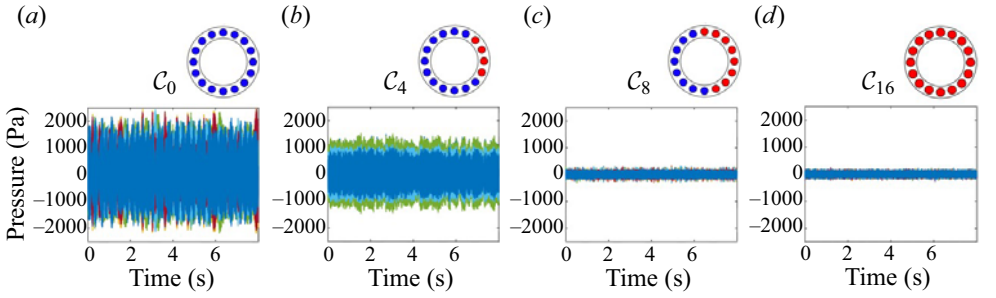

Figure 5. Pressure time series in the MICCA-Spray annular combustor for four configurations: (*a*) $\mathcal{C}_0$, (*b*) $\mathcal{C}_4$, (*c*) $\mathcal{C}_8$ and (*d*) $\mathcal{C}_{16}$. Experiments are carried out at a thermal power $\mathcal{P} = 118$ kW and a global equivalence ratio $\phi = 0.9$.

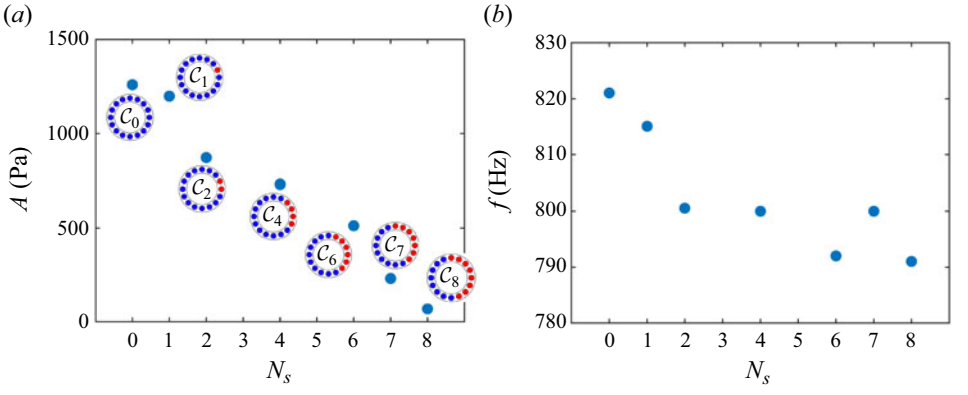

Figure 6. (*a*) Instability amplitude and (*b*) frequency as a function of the number N_s of *S*-injectors in MICCA-Spray, operated at a thermal power $\mathcal{P} = 118$ kW and a global equivalence ratio $\phi = 0.9$, for type $\mathcal{C}$ configurations.

When $N_s = 8$, pressure oscillations reach levels similar to those recorded in configuration $\mathcal{C}_{16}$ (around 100 Pa).

Figure 6 shows the level of pressure fluctuations in the chamber and the frequency of the instability as a function of the number of *S*-injectors. A gradual decrease in the pressure level is observed as N_s is increased. If one now looks at the frequencies, the values found are around 800 Hz, indicating that the mode involved in the combustion/acoustics coupling is the 1A1L mode of the annular chamber. The instability frequency decreases from 820 Hz to 790 Hz as the number of *S*-injectors in the chamber is augmented. The presence of the flames shifts the frequencies with respect to the eigenfrequency of the system without flames (which, in this case, was estimated to be 808 Hz for the 1A1L mode by taking a burnt gas temperature $T = 1500$ K). The change in frequency with the number of *S*-injectors in the system reflects modifications in the combustion/acoustics coupling linked to a progressively weaker combustion response as the number of *S*-injectors, characterized by FDFs that differ from those of *U*-injectors, is increased. This might also possibly be explained by a non-uniform azimuthal temperature distribution associated with the variation in equivalence ratio values due to the introduction of *S*-injectors in the system.

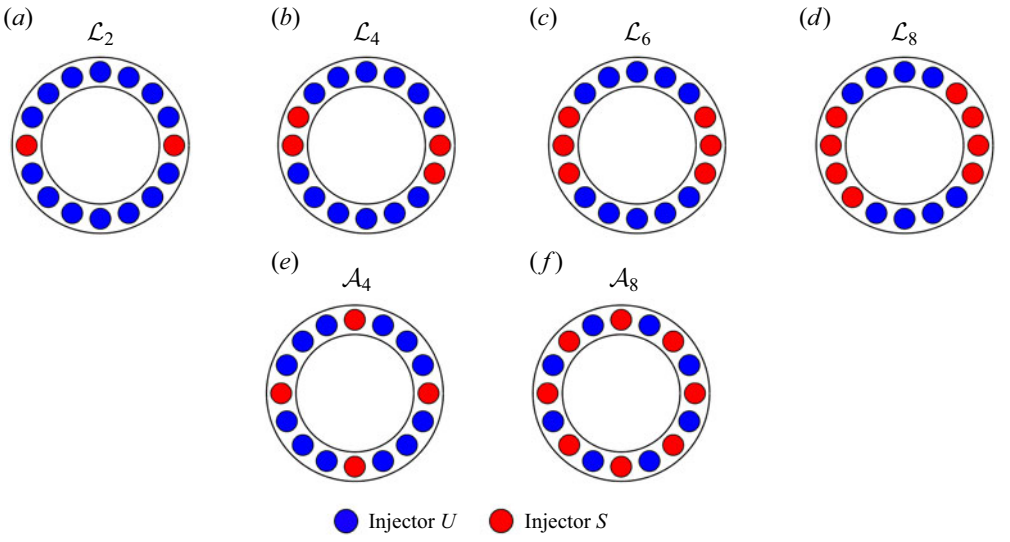

Figure 7. (*a–d*) Type $\mathcal{L}$ and (*e*,*f*) type $\mathcal{A}$ configurations investigated.

3.2. *Effects of the S-injector azimuthal locations*

In what follows, the number of *S*-injectors is fixed, and the effects of the relative position of these units are investigated by considering arrangements with 2, 4, 6 and 8 *S*-injectors. A first group of arrangements shown in figures 7(*a*)–7(*d*), denoted $\mathcal{L}_2$, $\mathcal{L}_4$, $\mathcal{L}_6$ and $\mathcal{L}_8$, respectively, corresponds to cases where the *S*-injectors are divided into two groups of equal size and placed on opposite sides of the annulus. For $N_s = 4$ and $N_s = 8$, a second category of arrangements, shown in figures 7(*e*) and 7(*f*), is also investigated, and will be denoted $\mathcal{A}_4$ and $\mathcal{A}_8$ to designate an alternation of *U*- and *S*-injectors.

Figures 8 and 9 show the arrangements investigated together with the pressure time series. These two figures indicate that, for a given number of *S*-injectors, 'face-to-face' (type $\mathcal{L}$) arrangements lead to higher levels of pressure fluctuations than 'side-by-side' (type $\mathcal{C}$) arrangements. In this respect, the case with eight *S*-injectors is particularly interesting (figure 8*c–e*). Arrangements where the eight *S*-injectors are gathered on one side of the chamber ($\mathcal{C}_8$) or for which there is an alternation between injectors *S* and *U* ($\mathcal{A}_8$) lead to stable operation while arrangement $\mathcal{L}_8$ induces large amplitude oscillations, with pressure fluctuation levels similar to those recorded in the cases without *S*-injectors. For configurations with four *S*-injectors in the system (figure 9*c–e*), arrangement $\mathcal{A}_4$ enables a more efficient reduction of the oscillations amplitude than $\mathcal{C}_4$.

Figure 10 shows the amplitude of pressure fluctuations and the instability frequency as a function of the number of *S*-injectors for all the configurations tested. Compared with $\mathcal{C}$ configurations, $\mathcal{L}$ arrangements lead to a level of pressure fluctuations in the chamber higher than or very close to the reference level corresponding to the case where there are no *S*-injectors in the chamber ($N_s = 0$). For a fixed value of N_s, $\mathcal{A}$ configurations lead to a lower level of pressure fluctuations than $\mathcal{C}$ configurations. Instability frequencies are very close for $\mathcal{C}$ and $\mathcal{L}$ configurations, although the amplitudes of pressure fluctuations are relatively different.

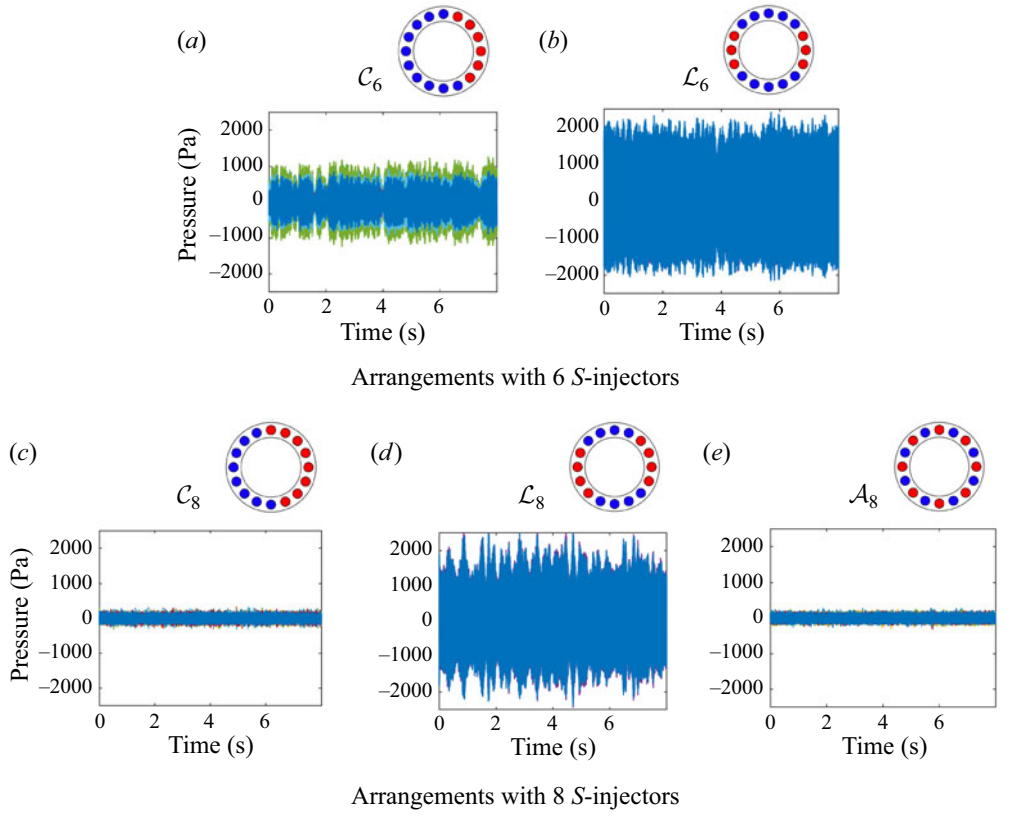

Figure 8. Pressure time series in the annular combustor MICCA-Spray, operated at a thermal power $\mathcal{P} = 118$ kW and a global equivalence ratio $\phi = 0.9$, for different configurations: (*a*) $\mathcal{C}_6$ and (*b*) $\mathcal{L}_6$, and (*c*) $\mathcal{C}_8$, (*d*) $\mathcal{L}_8$ and (*e*) $\mathcal{A}_8$.

3.3. *Effects of symmetry breaking on modal dynamics*

This section is aimed at examining the consequences of symmetry breaking on the modal dynamics in the annular system. It is worth, at this stage, to complement the review of the literature by briefly examining articles that deal with azimuthal mode dynamics and more specifically with the switching taking place between spinning, standing and mixed modes (Krebs *et al.* 2002; Bourgouin *et al.* 2013; Worth & Dawson 2013, 2017; Prieur *et al.* 2017; Mazur *et al.* 2019). It is also found that this switching prevails in numerical simulations (Wolf *et al.* 2012) and that the frequency of this phenomenon is relatively low compared with the acoustic frequency scale (Worth & Dawson 2017).

These questions are actively investigated on the theoretical level, and models are developed to explain why some modes are preferred. Ghirardo & Juniper (2013) extended the model proposed by Noiray *et al.* (2011) by taking into account the effects of acoustic azimuthal velocity on the flames. Noiray & Schuermans (2013) showed that mode switching can be explained by introducing stochastic noise forcing in analytical models of annular systems. Another question of interest concerns the preferred location of the nodal line in rotationally symmetric annular combustors when the standing mode prevails. An attempt to explain these observations is made by considering spontaneous breaking of rotational and reflectional symmetries in the system (Indlekofer *et al.* 2022). Another theoretical description of the dynamics of azimuthal waves is proposed by Faure-Beaulieu

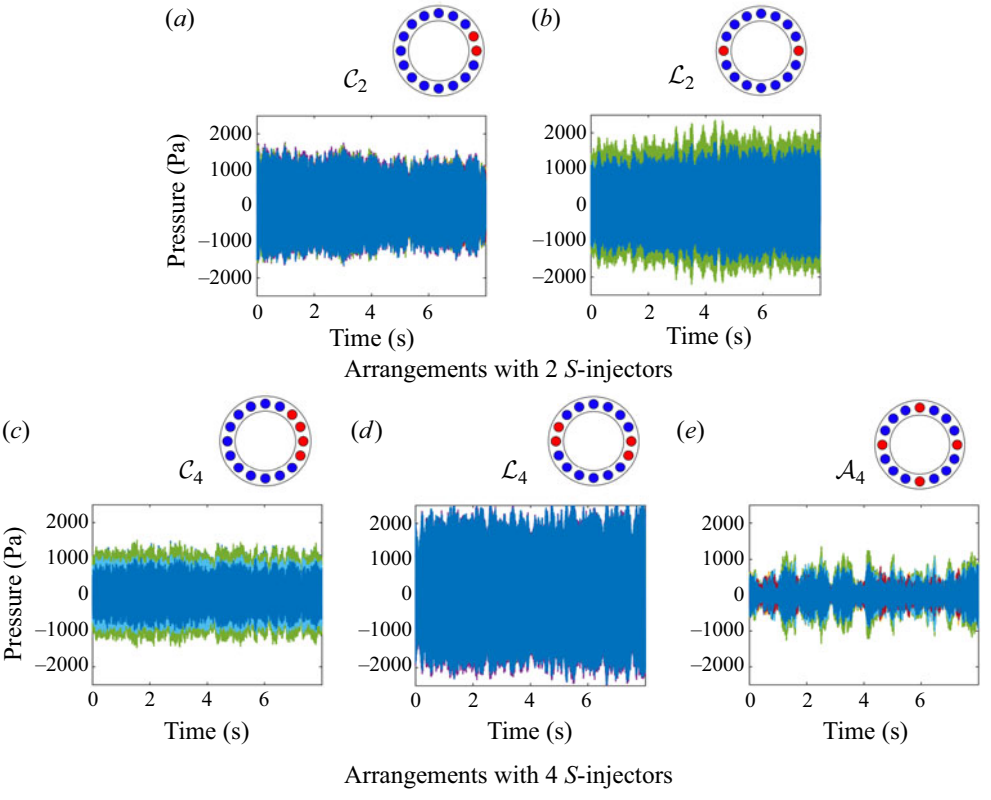

Figure 9. Pressure time series in the annular combustor MICCA-Spray, operated at a thermal power $\mathcal{P} = 118$ kW and a global equivalence ratio $\phi = 0.9$, for different configurations: (*a*) $\mathcal{C}_2$ and (*b*) $\mathcal{L}_2$, and (*c*) $\mathcal{C}_4$, (*d*) $\mathcal{L}_4$ and (*e*) $\mathcal{A}_4$.

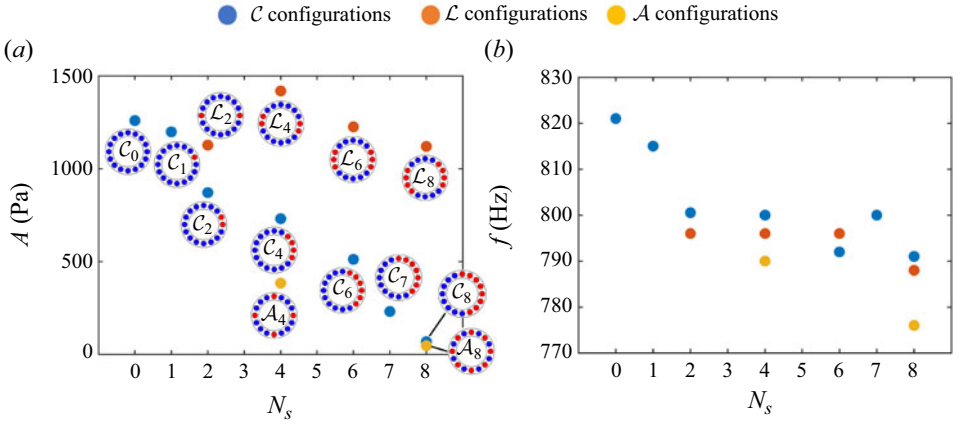

Figure 10. (*a*) Instability amplitude and (*b*) frequency as a function of the number of *S*-injectors in MICCA-Spray, N_s, for different configurations: $\mathcal{C}$ (blue), $\mathcal{L}$ (orange) and $\mathcal{A}$ (yellow). Experiments are carried out at an operating point of thermal power $\mathcal{P} = 118$ kW and an equivalence ratio $\phi = 0.9$.

& Noiray (2020) who show that the nature of the mode can be portrayed by making use of three slow-state variables, namely the amplitude, nature angle and nodal line angle. Symmetry breaking in azimuthal combustion dynamics is also analysed by Ghirardo *et al.* (2021) by making use of the method of averaging and considering small departures in the flame response gain with respect to baseline symmetric values.

Effects of symmetry breaking on modal dynamics in an annular system and on the nodal line position have been investigated in laboratory scale annular configurations. Experiments in the annular Rijke tube showed that the position of the nodal line coincides with the position of the heating grids with the lowest power for some staging patterns (Moeck *et al.* 2010). Dawson & Worth (2015) observed that placing baffles in the NTNU annular combustor chamber led to preferred standing modes whereas a configuration without baffles featured a permanent switching between standing and spinning modes. Symmetry breaking experiments in MICCA equipped with matrix burners showed that the orientation of the nodal line is controlled by the asymmetry pattern introduced in the system (Aguilar *et al.* 2021).

It is also worth recalling that modal dynamics can be described using the spin ratio, s_r, introduced by Bourgouin *et al.* (2013), which can be deduced from the wave amplitudes A_+ and A_-:

$$s_r = \frac{|A_+| - |A_-|}{|A_+| + |A_-|}. \tag{3.1}$$

A pure standing mode corresponds to the case where $A_+ = A_-$, such that $s_r = 0$. For a spinning mode in the clockwise (respectively counterclockwise) direction, $A_+ = 0$ (respectively $A_- = 0$) and the corresponding spin ratio is $s_r = -1$ (respectively $s_r = +1$). This spin ratio definition is close to that formulated by Evesque, Polifke & Pankiewitz (2003) based on acoustic energy considerations, but this earlier proposal does not distinguish between clockwise and counterclockwise spinning motions. Another representation based on the quaternion variables (Ghirardo & Bothien 2018) is also possible. It can be shown that the spin ratio is related to the 'nature angle', χ, by $s_r = \tan\chi$.

An interesting visualization of the modal characteristics consists in plotting the joint probability density function (j.p.d.f.), $p(A_+, A_-)$, calculated over a time series of the pressure field in the annular system. This is exemplified in figure 11 where this j.p.d.f. is shown for different configurations of U and S injection units.

In these plots, the distinction between standing and spinning modes is that proposed by Worth & Dawson (2013).

(i) If $A_+/A_- < 1/2$ (i.e. $-1 < s_r < -1/3$), the mode is deemed as clockwise spinning.
(ii) If $1/2 < A_+/A_- < 2$ (i.e. $-1/3 < s_r < 1/3$), the mode is deemed as standing.
(iii) If $A_+/A_- > 2$ (i.e. $1/3 < s_r < 1$), the mode is deemed as counterclockwise spinning.

When there are no S-injectors in the system (configuration $\mathcal{C}_0$), A_+ and A_- take a wide range of values, and a broad region of the $\{A_+, A_-\}$ plane is explored by the system: the mode switches from spinning to standing at a frequency of the order of a few Hz. When one S-injector is added (configuration $\mathcal{C}_1$), a preferred spinning mode in the counterclockwise direction is observed. When two or more S-injectors are present (configurations $\mathcal{C}_2$, $\mathcal{C}_4$, $\mathcal{C}_6$, $\mathcal{L}_2$, $\mathcal{L}_4$, $\mathcal{L}_6$ and $\mathcal{L}_8$), a standing mode is preferred, as points of highest probability density function value lie within the two dashed lines separating the standing mode from the spinning modes.

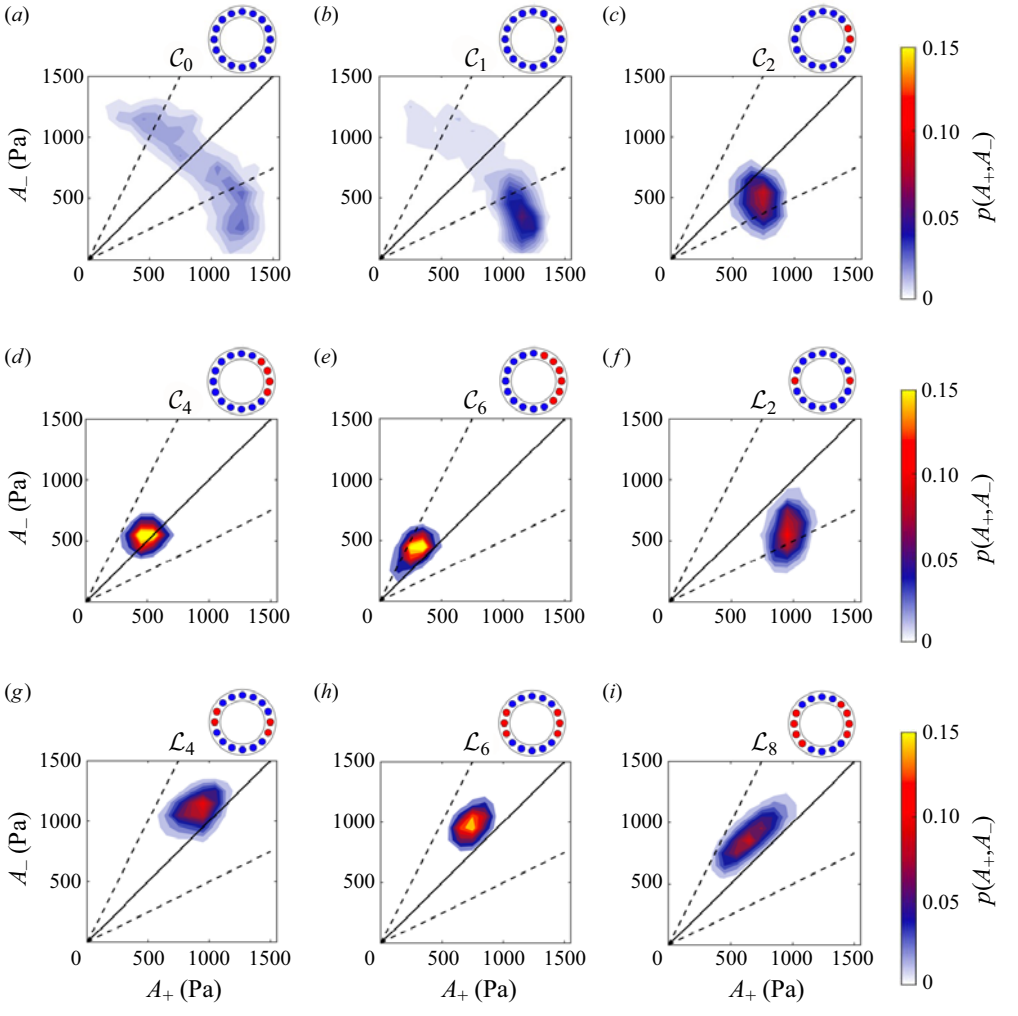

Figure 11. Joint probability density functions of A_+ and A_-, $p(A_+, A_-)$, determined from pressure time series: (*a*) $\mathcal{C}_0$, (*b*) $\mathcal{C}_1$, (*c*) $\mathcal{C}_2$, (*d*) $\mathcal{C}_4$, (*e*) $\mathcal{C}_6$, (*f*) $\mathcal{L}_2$, (*g*) $\mathcal{L}_4$, (*h*) $\mathcal{L}_6$ and (*i*) $\mathcal{L}_8$. Dashed lines, corresponding to $A_+/A_- = 1/2$ and $A_+/A_- = 2$, separate the standing mode from the spinning modes in the clockwise and counterclockwise directions.

The location of the *S*-injectors imposes the orientation of the nodal line, as can be seen from the pressure recordings for configurations $\mathcal{C}_0$, $\mathcal{C}_8$, $\mathcal{C}_4$ and $\mathcal{L}_4$ presented in figure 12. For configuration $\mathcal{C}_0$, which constitutes a reference unstable case, all the microphones record similar levels of pressure fluctuations. For configurations $\mathcal{C}_4$ and $\mathcal{L}_4$, the positions where the microphones recorded the lowest pressure fluctuations coincide with those of the *S*-injectors. Using these microphone recordings, the pressure field can be reconstructed using (2.4), and the position of the nodal line (where the pressure fluctuations are the lowest) can be determined.

Nodal line distributions are displayed in figure 13 for configurations $\mathcal{C}_2$, $\mathcal{C}_4$, $\mathcal{L}_2$ and $\mathcal{L}_4$. They show narrower distributions for configurations $\mathcal{C}_4$ and $\mathcal{L}_4$ than for $\mathcal{C}_2$ and $\mathcal{L}_2$. Another way to analyse the nodal line position consists in representing the probability of the nodal line location in the annular geometry, determined from the nodal line

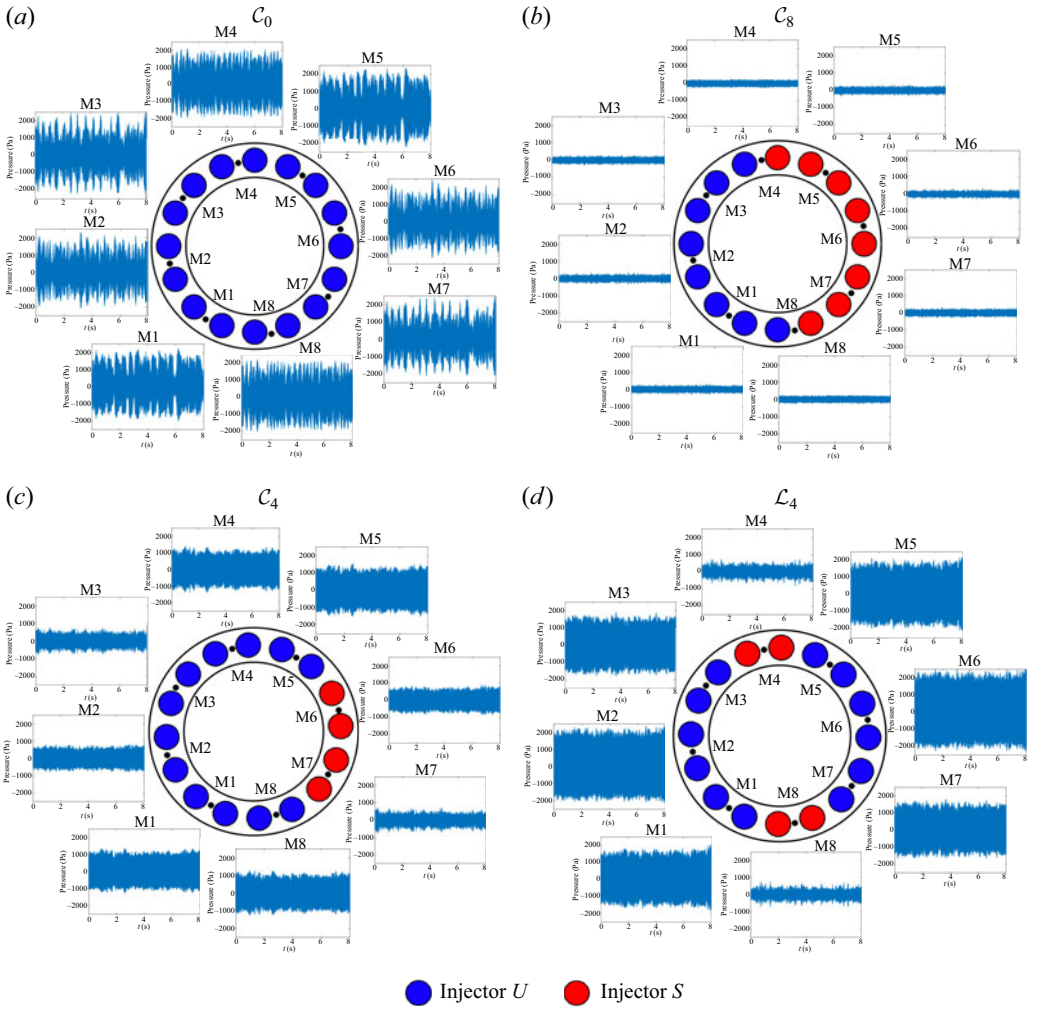

Figure 12. Pressure time series at different microphone positions for configurations: (*a*) $\mathcal{C}_0$; (*b*) $\mathcal{C}_8$; (*c*) $\mathcal{C}_4$; and (*d*) $\mathcal{L}_4$.

distribution, as illustrated in figure 13(*f–i*). For configuration $\mathcal{C}_2$, the nodal line passes through the *S*-injectors, and for configurations $\mathcal{C}_4$ and $\mathcal{L}_4$, the nodal line shows a preferred location between two injectors, closer to an injector than to another neighbour of the same type. When there is a single *S*-injector or when an odd number of *S*-injectors is in a $\mathcal{C}$ configuration, the nodal line passes respectively through the unique injector or through the central unit in the $\mathcal{C}$ arrangement. These findings generally correspond to what one might expect on a physical basis, but it is worth trying to explain what is observed by calculating the growth rates associated with the different configurations and showing that the nodal line location is that corresponding to a maximum in the growth rate (see § 4.3).

4. Interpretation using acoustic energy balance equations and flame describing functions

It is now interesting to see if the previous experimental observations can be interpreted in a unified framework. Results obtained suggest that it might be possible to derive a framework that could suitably represent changes in the injection units by making use

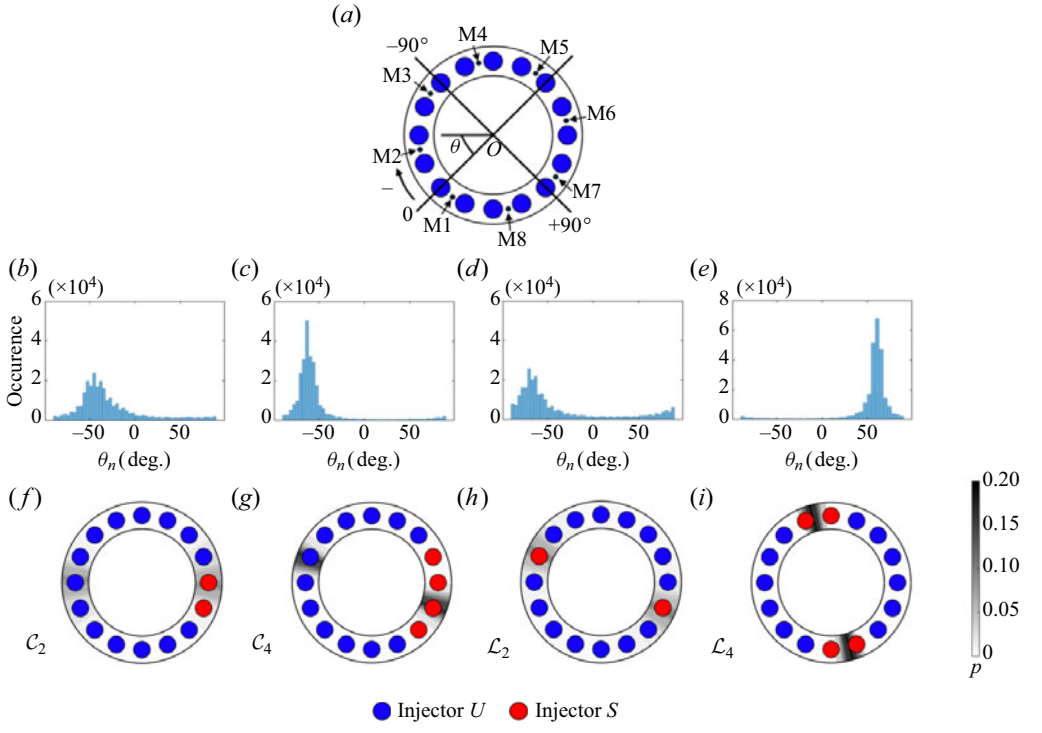

Figure 13. Nodal line positions for four staging patterns. (*a*) Origin and sign of the angles. Nodal line distribution (with a bin size of 4.5 °) for configurations: (*b*) $\mathcal{C}_2$; (*c*) $\mathcal{C}_4$; (*d*) $\mathcal{L}_2$; and (*e*) $\mathcal{L}_4$. Probability of the nodal line position for configurations: (*f*) $\mathcal{C}_2$; (*g*) $\mathcal{C}_4$; (*h*) $\mathcal{L}_2$; and (*i*) $\mathcal{L}_4$.

of the acoustic energy balance applied to the annular geometry. This possibility will be explored in what follows by making use of the assumption that the various injection units operate independently from each other and that their flame describing functions may be assimilated to those measured in the single sector experiments and displayed in § 2. This hypothesis is validated by the results obtained by Patat *et al.* (2021) in a set-up comprising a rectangular combustion chamber equipped with injector units identical to those used in the present study. The authors showed, by submitting an array of flames to transverse acoustic oscillations, that the FDF of a flame placed at a pressure anti-nodal line is similar to the FDF of a flame at an intermediate position between a pressure node and a pressure anti-node if they are submitted to the same pressure oscillation at the outlet of the injector. The azimuthal flow modifies the lateral dynamics but does not change the FDF, which essentially results from the axial dynamics. The FDF measured in the single injector configuration SICCA-Spray can hence be used to interpret the observations in MICCA-Spray. However, if the flames' spacings were smaller, with strong interactions between the flames' fronts, this hypothesis might probably not be valid any longer.

If one now considers that the flames formed by the various injectors operate independently from each other, it is possible to derive an expression of the source term based on the FDFs of the flames formed by the two types of injectors. This will be a function of the number of injectors N_s and N_u, and of their position in the annular system. This analysis will serve two purposes. First, obtain an estimate of the growth rate for the different configurations investigated. Knowing which configurations are stable and unstable will also enable to identify upper and lower bounds for the damping rate of the

annular system. The second objective is to explain the nodal line locking in a preferred position observed for some configurations, by comparing the growth rates corresponding to different nodal line positions.

4.1. *Acoustic energy balance framework*

One seeks an analytical expression for the growth rate, as a function of the FDFs of the two types of injectors and their relative position in the annulus. The starting point of this analysis is the acoustic energy balance equation, which reads

$$\frac{\partial \mathcal{E}}{\partial t} + \boldsymbol{\nabla} \cdot \boldsymbol{\mathcal{F}}_a = \mathcal{S} - \mathcal{D}, \tag{4.1}$$

where $\mathcal{E}$, $\boldsymbol{\mathcal{F}}_a$, $\mathcal{S}$ and $\mathcal{D}$ are the instantaneous acoustic energy density, the acoustic energy flux, the Rayleigh source term and the volumetric damping term, respectively,

$$\mathcal{E} = \frac{1}{2}\frac{p'^2}{\rho_0 c^2} + \frac{1}{2}\rho_0 v'^2 \tag{4.2}$$

$$\boldsymbol{\mathcal{F}}_a = p'\boldsymbol{v}' \tag{4.3}$$

$$\mathcal{S} = \frac{\gamma - 1}{\rho_0 c^2} p' \dot{q}' \tag{4.4}$$

with p', $\boldsymbol{v}'$ the acoustic pressure and velocity, $\dot{q}'$ the heat release rate fluctuations, ρ_0 the ambient density, c the speed of sound and γ the specific heat ratio.

In the case of harmonic oscillations, spatial and temporal variations may be decoupled, and one can write

$$p' = Re\{\tilde{p}(t)\mathrm{e}^{-\mathrm{i}\omega t}\}, \quad \boldsymbol{v}' = Re\{\tilde{\boldsymbol{v}}(t)\mathrm{e}^{-\mathrm{i}\omega t}\}, \quad \dot{q}' = Re\{\tilde{\dot{q}}(t)\mathrm{e}^{-\mathrm{i}\omega t}\}, \tag{4.5a–c}$$

where $\tilde{p}(t)$, $\tilde{\boldsymbol{v}}(t)$ and $\tilde{\dot{q}}(t)$ are slowly varying functions, and $\omega = 2\pi f$, with f the frequency of oscillation.

Integrating the balance equation over a period of oscillation yields an equation linking period averages:

$$\frac{\partial E}{\partial t} + \boldsymbol{\nabla} \cdot \boldsymbol{F} = S - D, \tag{4.6}$$

where E, $\boldsymbol{F}$ and S are the period averages of $\mathcal{E}$, $\boldsymbol{\mathcal{F}}_a$ and $\mathcal{S}$. These quantities are conveniently determined with (4.7), valid if the slowly varying variables can be assumed constant over a cycle of oscillation

$$\frac{1}{T}\int_{[T]} a'b' \,\mathrm{d}t = \frac{1}{2} Re\{\tilde{a}\tilde{b}^*\} \tag{4.7}$$

with $a' = Re\{\tilde{a}(t)\mathrm{e}^{-\mathrm{i}\omega t}\}$, $b' = Re\{\tilde{b}(t)\mathrm{e}^{-\mathrm{i}\omega t}\}$ and * designating the complex conjugate. One hence obtains

$$E = \frac{1}{4}\frac{\tilde{p}\tilde{p}^*}{\rho_0 c^2} + \frac{1}{4}\rho_0 \tilde{\boldsymbol{v}} \cdot \tilde{\boldsymbol{v}}^*, \tag{4.8}$$

$$\boldsymbol{F} = \tfrac{1}{2} Re\{\tilde{p}\tilde{\boldsymbol{v}}^*\}, \tag{4.9}$$

$$S = \frac{\gamma - 1}{\rho_0 c^2}\frac{1}{2} Re\{\tilde{p}\tilde{\dot{q}}^*\}. \tag{4.10}$$

Taking the average of the balance equation over the volume V of the combustor, one gets

$$\frac{\mathrm{d}\langle E\rangle}{\mathrm{d}t} = \langle S\rangle - \langle D\rangle - \langle F\rangle \tag{4.11}$$

with $\langle E\rangle$, $\langle S\rangle$ and $\langle D\rangle$ the integrals over the volume V of E, S and D, and $\langle F\rangle = \int_A \boldsymbol{F}\cdot\boldsymbol{n}\,\mathrm{d}A$ the surface integral of the normal energy flux.

Assuming that p', $\boldsymbol{v}'$ and $\dot{q}'$ have a common term $\exp(-\mathrm{i}\omega t)$, with $\omega = \omega_r + \mathrm{i}\omega_i'$, where ω_r is the angular frequency and ω_i' represents the effective growth or decay rate of the oscillations, one can divide (4.11) by $2\langle E\rangle$ to identify a growth rate ω_i and a damping rate α:

$$\omega_i = \frac{1}{2\langle E\rangle}\langle S\rangle \tag{4.12}$$

$$\alpha = \frac{1}{2\langle E\rangle}[\langle D\rangle + \langle F\rangle] \tag{4.13}$$

such that $\omega_i' = \omega_i - \alpha$ represents the effective growth rate, determining whether the oscillation will grow or decay. Here, ω_i corresponds to the growth rate in the absence of damping and this term can take positive or negative values; α is the damping rate, resulting from sources of acoustic energy dissipation in the control volume and acoustic energy fluxes escaping the volume and inducing a rate of change of the acoustic energy in the volume. Assuming that the boundaries are only passive (that the acoustic flux leaving the volume is always positive or null), the damping rate α is always positive and the oscillation will grow if $\omega_i > \alpha$.

To determine ω_i, one now has to calculate the period average of the Rayleigh source term

$$\langle S\rangle = \frac{\gamma-1}{\rho_0 c^2}\frac{1}{T}\int_{[T],V} p'\dot{q}'\,\mathrm{d}V\,\mathrm{d}t. \tag{4.14}$$

Introducing the volume integrated heat release rate fluctuations $\dot{Q} = \int_V \dot{q}'\,\mathrm{d}V$, and assuming that the pressure is constant in the region where there are heat release rate fluctuations, i.e. that the flames are compact with respect to the acoustic wavelength, one gets

$$\langle S\rangle = \dot{Q}_0\frac{\gamma-1}{\gamma}\frac{1}{T}\int_{[T]}\frac{p'}{p_0}\frac{\dot{Q}'}{\dot{Q}_0}\,\mathrm{d}t, \tag{4.15}$$

which can be rewritten as

$$\langle S\rangle = \dot{Q}_0\frac{\gamma-1}{\gamma}\frac{1}{2}Re\left\{\frac{\tilde{p}}{p_0}\left[\frac{\widetilde{\dot{Q}'}}{\dot{Q}_0}\right]^*\right\}. \tag{4.16}$$

One now seeks an analytical expression for the relative heat release rate fluctuations, $\widetilde{\dot{Q}'}/\dot{Q}_0$. Introducing the flame describing function, $\mathcal{F}$, linking relative heat release rate

fluctuations to relative velocity fluctuations,

$$\mathcal{F} = \frac{\widetilde{\dot{Q}'}/\dot{Q}_0}{\tilde{v}/\bar{v}} \tag{4.17}$$

and using the effective impedance, ζ, to link relative velocity fluctuations to relative pressure fluctuations at the flame position, one gets

$$\frac{\widetilde{\dot{Q}'}}{\dot{Q}_0} = \mathcal{F}\frac{1}{\bar{v}}\frac{\tilde{p}}{\rho_0 c\zeta} = \frac{\mathcal{F}}{\zeta}\frac{1}{\gamma M}\frac{\tilde{p}}{p_0}, \tag{4.18}$$

where M is the Mach number of the flow at the flame.

Introducing $\mathcal{F} = G_F \mathrm{e}^{\mathrm{i}\varphi_F}$ and $\zeta = G_\zeta \mathrm{e}^{\mathrm{i}\varphi_\zeta}$, one can write the relative heat release rate fluctuations in the following form:

$$\frac{\widetilde{\dot{Q}'}}{\dot{Q}_0} = \frac{G_F}{G_\zeta}\frac{1}{\gamma M}\frac{\tilde{p}}{p_0}\exp(\mathrm{i}\varphi_F - \mathrm{i}\varphi_\zeta). \tag{4.19}$$

In the case of an annular combustor, assuming that the 1A1L mode is involved in the coupling and considering a mixed azimuthal structure, pressure fluctuations can be cast in the form

$$\tilde{p}(x,\theta) = [a\exp(\mathrm{i}\theta - \mathrm{i}\omega t) + b\exp(-\mathrm{i}\theta - \mathrm{i}\omega t)]\psi(x). \tag{4.20}$$

To simplify notation, the complex amplitudes A_+ and A_- of (2.4) have been replaced by a and b. As already indicated in § 2, (4.20) constitutes an approximate representation of the pressure field that neglects distortions induced by circumferential staging in the 1A azimuthal modal structure.

The axial wavefunction corresponding to the 1L mode is $\psi(x) = \cos[\pi x/(2l)]$. It is assumed that the flames are compact with respect to the acoustic wavelength, and one may neglect any variation in the axial direction and assume that the axial wavefunction takes a constant value at the flame position, $\psi(x) \simeq \psi(x_f)$, and simply designate this value by ψ_f.

The volume integrated period average contribution of the jth flame, located at an azimuthal angle θ_j, to the source term using (4.16) writes:

$$\langle S_j\rangle = \frac{1}{2}\frac{(\gamma-1)}{\gamma}\dot{Q}_0\frac{1}{\gamma p_0^2}\frac{1}{M}\frac{G_F}{G_\zeta}\psi_f^2 Re(J), \tag{4.21}$$

where

$$J = (a\mathrm{e}^{\mathrm{i}\theta} + b\mathrm{e}^{-\mathrm{i}\theta})(a^*\mathrm{e}^{-\mathrm{i}\theta} + b^*\mathrm{e}^{\mathrm{i}\theta})\mathrm{e}^{-\mathrm{i}(\varphi_j - \varphi_\zeta)}. \tag{4.22}$$

Rewriting

$$a = |a|\mathrm{e}^{\mathrm{i}\Phi_+}, \quad b = |b|\mathrm{e}^{\mathrm{i}\Phi_-} \tag{4.23a,b}$$

and introducing

$$\theta_0 = (\Phi_- - \Phi_+)/2, \tag{4.24}$$

which corresponds to the 'spatial phase' term determining the pressure anti-node location in the quaternion representation (Ghirardo & Bothien 2018) (this is easily verified, for

example, in the case of a standing mode by taking $|a| = |b|$), one obtains, after a few calculations,

$$\langle S_j \rangle = \frac{1}{2}\frac{(\gamma-1)}{\gamma}\dot{Q}_0\frac{1}{\gamma p_0^2}\frac{1}{M}\frac{G_F}{G_\zeta}\psi_f^2\cos(\varphi_j-\varphi_\zeta)\left[|a|^2+|b|^2+2|a||b|\cos(2(\theta-\theta_0))\right]. \tag{4.25}$$

Now the acoustic energy integrated over a period and the combustor volume reads

$$\langle E \rangle = \int_V \left[\frac{1}{4}\frac{\tilde{p}\tilde{p}^*}{\rho_0 c^2}+\frac{1}{4}\rho_0\tilde{\boldsymbol{v}}\cdot\tilde{\boldsymbol{v}}^*\right]\mathrm{d}V, \tag{4.26}$$

which can be simplified into

$$\langle E \rangle = \frac{1}{4}\frac{1}{\rho_0 c^2}[|a|^2+|b|^2]V. \tag{4.27}$$

Using the growth rate expression (4.12) and making use of the assumption that the different injectors operate independently from each other, one may write

$$\omega_i = \frac{1}{2\langle E \rangle}\sum_{j=1}^{N}\langle S_j \rangle, \tag{4.28}$$

which yields, after insertion of (4.25) and (4.27):

$$\omega_i = \frac{(\gamma-1)}{\gamma}\frac{\dot{Q}_0}{p_0 V}\psi_f^2\sum_{j=1}^{N}\frac{G_{Fj}}{MG_{\zeta j}}\cos(\varphi_{Fj}-\varphi_{\zeta j})\left[1+\frac{2|a||b|}{|a|^2+|b|^2}\cos(2(\theta_j-\theta_0))\right]. \tag{4.29}$$

The growth rate appears like a weighted sum of the contributions of the individual flames depending on the position of the injectors with respect to the pressure anti-nodal line position (θ_0), appearing in the $\cos(2(\theta_j-\theta_0))$ term. It also depends on the phase difference between the flame describing functions and the phase of the specific impedance that links the pressure and velocity disturbances acting on the flame through the $\cos(\varphi_{Fj}-\varphi_{\zeta j})$ term, and on the gain of the FDFs of the various types of injectors.

It is first interesting to consider a case where all injectors have the same FDF and impedance gain and phase values, i.e. when $G_{Fj}=G_F$, $\varphi_{Fj}=\varphi_F$, $G_{\zeta j}=G_\zeta$ and $\varphi_{\zeta j}=\varphi_\zeta$. In that case, one finds that the second term in the brackets in expression (4.29) does not contribute to the sum over the N injectors and one obtains

$$\omega_i = \frac{(\gamma-1)}{\gamma}\frac{N\dot{Q}_0}{p_0 V}\psi_f^2\frac{G_F}{MG_\zeta}\cos(\varphi_F-\varphi_\zeta). \tag{4.30}$$

In this particular case of identical flame responses for all the injectors, one finds that the growth rate does not depend on the nature of the mode that assures the coupling, and that ω_i is the same for mixed, CCW or CW spinning, and standing modes. This definitely explains experimental observations where these various modes appear and continuously switch between the various possible amplitudes of the CCW and CW composing the azimuthal structure. This ceases to be true when injectors feature different responses characterized by differences in the gains G_F and phases φ_F.

It is also interesting to consider two limiting cases corresponding to a standing mode and a pure spinning mode. In the first case, $|a| = |b|$, and (4.29) becomes

$$\omega_i = 2(\gamma - 1)\frac{\dot{Q}_0}{\gamma p_0 V}\psi_f^2 \sum_{j=1}^{N} \frac{G_{Fj}}{MG_{\zeta j}} \cos(\varphi_{Fj} - \varphi_{\zeta j}) \cos^2(\theta_j - \theta_0). \tag{4.31}$$

In the latter expression, the $G_{Fj}\cos(\varphi_{Fj} - \varphi_{\zeta j})$ term associated with each flame is weighted by the $\cos^2(\theta_j - \theta_0)$ term, depending on the position of the flame with respect to the anti-nodal line.

In the second case, one of the wave amplitudes a or b vanishes and the growth rate takes the form:

$$\omega_i = (\gamma - 1)\frac{\dot{Q}_0}{\gamma p_0 V}\psi_f^2 \sum_{j=1}^{N} \frac{G_{Fj}}{MG_{\zeta j}} \cos(\varphi_{Fj} - \varphi_{\zeta j}). \tag{4.32}$$

If the mode is spinning, the contribution of each flame to the total growth rate is independent of its position in the annular system.

4.2. *Validation of the analytical framework*

The objective of the present section is to validate the analytical framework with two test cases before using it to determine the growth rates for all the configurations investigated. To do so, it is convenient to work with the dimensionless quantity $\langle S_j \rangle / \dot{Q}_0$, the source term at flame j divided by the mean heat release rate in one flame, since it can be determined experimentally from simultaneous pressure and photomultiplier recordings using (4.15) recalled below as

$$\langle S_j \rangle / \dot{Q}_0 = \frac{\gamma - 1}{\gamma}\frac{1}{T}\int_{[T]} \frac{p_j'}{p_0}\frac{\dot{Q}'}{\dot{Q}_0}\,\mathrm{d}t. \tag{4.33}$$

The flames behaving in a quasi-premixed fashion (see § 2.2), the relative heat release rate fluctuations can be approximated by the relative intensity fluctuations recorded by a photomultiplier equipped with an OH* filter, $I'/I \approx \dot{Q}'/\dot{Q}_0$.

The source term at the jth flame can also be determined analytically and expressed as a function of the level of peak pressure fluctuations in the chamber at injector j, $|p_j'/p_0|^2$, by combining (4.16) and (4.19) as

$$\langle S_j \rangle / \dot{Q}_0 = \frac{1}{2}\frac{\gamma - 1}{\gamma^2}\frac{G_{Fj}}{G_{\zeta j}}\frac{1}{M}\left|\frac{p_j'}{p_0}\right|^2 \cos(\varphi_{Fj} - \varphi_{\zeta j}). \tag{4.34}$$

The level of peak pressure fluctuations at injector j, $|p_j'/p_0|^2$, constitutes a data input from experiments for this validation case.

The experimental set-up used for this study is presented in figure 14(*a*,*d*). Eight photomultipliers record the relative light intensity fluctuations emitted by eight adjacent flames on one half of the annulus. Pressure fluctuations are reconstructed at each injector position using pressure recordings and (2.4). The values of $\langle S_j \rangle / \dot{Q}_0$ thus obtained experimentally and analytically for eight flames will be compared for two configurations leading to a well-defined standing mode with the nodal line location controlled by the position of S-injectors: $\mathcal{L}_4$ and a variation of configuration $\mathcal{L}_4$, denoted $\mathcal{L}_{4+1}$, in which an additional S-injector was placed close to the pressure anti-node.

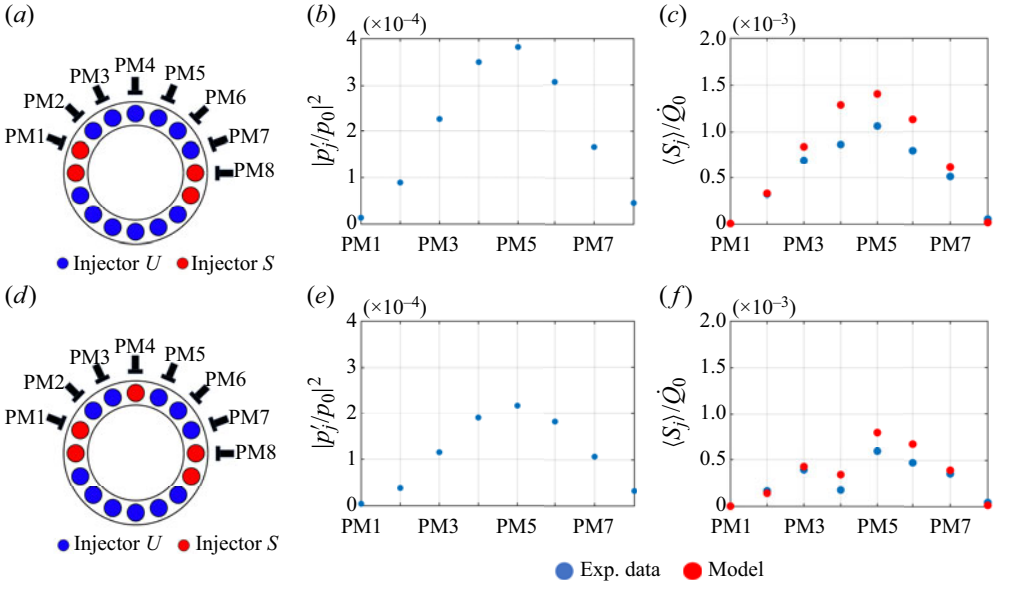

Figure 14. Experimental validation of the analytical framework: (*a–c*) configurations $\mathcal{L}_4$ and (*d–f*) $\mathcal{L}_{4+1}$. (*a*,*d*) Experimental set-up, with the positions of the *U*- and *S*-injectors and the photomultipliers (denoted 'PMX'). (*b*,*e*) Peak pressure fluctuations $|p'_j/p_0|^2$ at the eight photomultiplier locations. (*c*,*f*) Comparison between $\langle S_j\rangle/\dot{Q}_0$ determined experimentally (blue) and analytically (red) at the eight photomultiplier positions.

Parameter	Determination procedure
N	Number of injectors in the annular system (here $N = 16$).
θ_j	Location of the jth injector: $\theta_j = (j-1)2\pi/N$.
θ_0	Pressure anti-nodal line location.
V	Volume of the annular chamber $V = \mathcal{P}_a l_a l$, with $\mathcal{P}_a$ the annulus mean perimeter, l_a the annulus width, and l the quartz walls length.
$\dot{Q}_0$	Mean heat release rate in one flame.
ψ_f	Value of the axial eigenfunction determined at x_f: $\psi = \psi_1(x_f) = \cos(\pi x_f/(2l))$.
G_{Fj}, φ_{Fj}	Gain and phase of the FDF determined at the frequency of the 1A1L mode, f_{11}: $G_{Fj} = G_{Fj}(f_{11})$, $\varphi_{Fj} = \varphi_{Fj}(f_{11})$.
φ_ζ	Phase of the specific impedance at the flame determined with the method described in Appendix B.
MG_ζ	Product of the Mach number at the flame (M) by the specific impedance gain (G_ζ) determined with the method described in Appendix B.
$\lvert p'_j/p_0\rvert^2$	Level of peak pressure fluctuations at injector j, determined from measurements with the microphones flush-mounted on the backplane of the chamber.
p_0	Ambient pressure, 10^5 Pa.
γ	Specific heat ratio, $\gamma = 1.4$.

Table 2. Parameters used for the growth rate calculations and procedure employed to determine these quantities.

The different quantities appearing in the source term expression and the methodology used to determine them are gathered in table 2. The gain and phase values of the FDF are obtained from the FDF measurements presented in § 2.2. FDF gain and phase are evaluated at the frequency $f_{11} = 808$ Hz, corresponding to the eigenvalue of the 1A1L mode of the MICCA-Spray combustion chamber calculated by (2.3). The impedance phase φ_ζ and the

product MG_ζ are determined with the procedure described in Appendix B. It is also shown that the impedances ζ_U and ζ_S of the different injection units are quite close. Although the respective pressure drop values of injectors U and S are different, their transfer matrices (discussed in Appendix B) are mainly determined by the air distributor and terminal plate which are common to the two types of injectors, the swirler only having a minor influence on the coefficients of these matrices. As a consequence, $\zeta_S \simeq \zeta_U$, and one may use the same effective impedance ζ.

The comparison between experimental data and the analytical determination of the source term is presented in figure 14(c,f). Experimental measurements for the source term show that the flames located at the pressure node do not contribute significantly to the total source term. The flames bringing the highest contribution are those located at the pressure anti-node. Placing a S-injector close to the pressure anti-node (configuration $\mathcal{L}_{4+1}$, figure 14d–f) induces a drop in the source term value at the position of the S-injector facing photomultiplier 'PM4'. This can be linked to the smaller FDF gain value measured for injector S, compared with that for injector U. A good qualitative and quantitative agreement between the experimental measurements and the evaluation of the analytical expression is found. The drop in the value of the source term observed for configuration $\mathcal{L}_{4+1}$ at the position of the S-injector facing photomultiplier 'PM4' is also well retrieved by the analytical expression of the source term.

4.3. *Nodal line locking*

The analytical expression of the growth rate is now used to interpret mode selection and nodal line locking phenomena.

At this point, it is first useful to recall theoretical results on how breaking the symmetry in an annular system changes the associated eigenvalues and modal structures. A perfectly symmetric annular combustor features degenerate eigenvalues. In this case, the mode structure is spinning, standing or of mixed type. Symmetry breaking induced by the staging of different injectors (or the introduction of Helmholtz resonators) splits the initially degenerate eigenvalue into a couple of distinct eigenvalues, characterized by different frequencies and growth rates (Stow & Dowling 2003; Bauerheim *et al.* 2014, 2015). It is found by Bauerheim *et al.* (2014) that staging two types of injectors in an annular system gives rise to standing modes with perpendicular nodal lines and introduces a 'splitting strength', controlling the difference between the eigenfrequencies and growth rates associated with the two modes. The latter quantity depends on the flame dynamical characteristics and the staging pattern.

One may now interpret the experimental results obtained in MICCA-Spray in light of these theoretical findings in combination with the analysis of the growth rate expressions for the different configurations. To that end, figure 15 shows the growth rate as a function of the nodal line location for all the configurations investigated. Power spectral densities (PSDs) of the pressure signals, together with nodal line angular positions and spin ratio time series, are also reported for unstable configurations in Appendix C to support the analysis carried out in this section.

Let us start with configurations $\mathcal{C}_0$ and $\mathcal{C}_{16}$, where all the injectors are of one type. Theoretically, the mode is degenerate. The power spectral densities of the pressure signals feature a single peak and mixed modes are observed experimentally with the nodal line position sweeping a broad range of locations (see Appendix C). The associated growth rate given by (4.31) shows no dependence on the nodal line position, which is coherent with the experimental observations. For case $\mathcal{C}_8$, the growth rate also does not show any variations with the nodal line location θ_n, and its value is half-way between those found

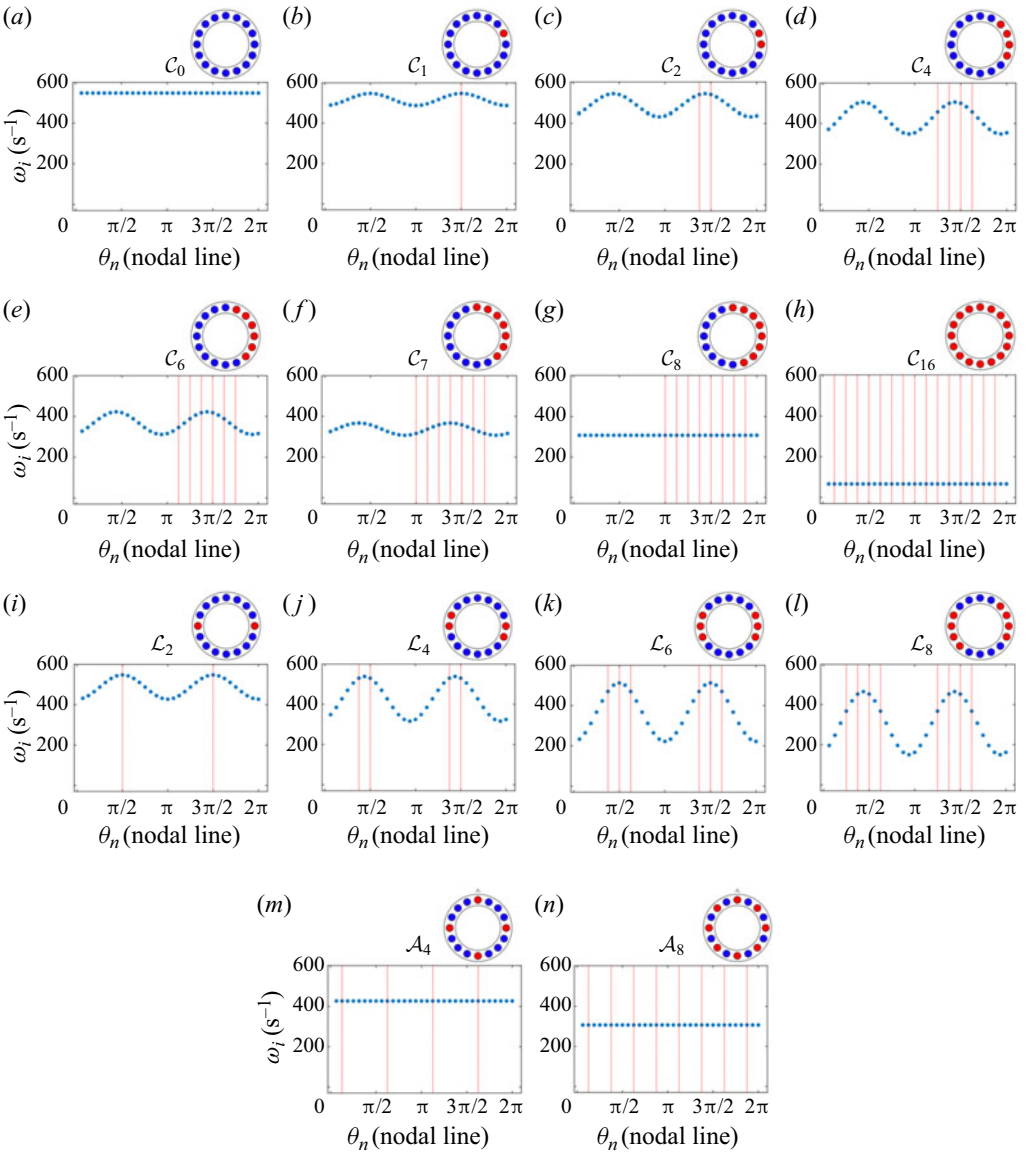

Figure 15. Growth rate ω_i as a function of the nodal line position θ_n for all the configurations investigated. Red vertical lines correspond to the position of S-injectors in the annular system. Although only two possible standing modes with perpendicular nodal line positions are theoretically predicted for cases $\mathcal{C}_2, \mathcal{C}_4, \mathcal{C}_6, \mathcal{L}_2, \mathcal{L}_4, \mathcal{L}_6$ and $\mathcal{L}_8$, the growth rate ω_i is evaluated for a range of nodal line positions θ_n to examine the change in shape of the function for these different staging patterns.

for $\mathcal{C}_0$ and $\mathcal{C}_{16}$, and probably lower than the damping rate since this case is found to be stable in the tests.

For configuration $\mathcal{C}_1$ where an S-injector replaces a U-injector, the mode is of mixed type and a single frequency peak is observed in the power spectral density (see the corresponding plots reported in Appendix C). The mathematical evaluation of (4.31) indicates a small difference between the minimum and maximum values of the growth rate. One may infer that, for this staging pattern, the splitting strength is low, giving rise to

a small loss of degeneracy, with a frequency difference between the two eigenmodes below the frequency resolution of the PSD ($\Delta f = 4$ Hz). In addition, the beating observed in the pressure signal at a frequency around 2 Hz, displayed in Appendix C, is another indication of this slight loss of degeneracy. It is also interesting to note that, in this particular configuration, the mixed modal structures are preferentially of the CCW spinning wave type. One might think that this preferred spinning direction could be linked to the tangential flow induced by the injection unit swirlers which are all oriented in the same direction. However, this global rotating flow is slow (Durox *et al.* 2015) and rotates in the CW direction. The statistical preference observed for the CCW mode in configuration $\mathcal{C}_1$ is probably not linked to the bulk swirl, as already discussed by Rajendram Soundararajan *et al.* (2022*a*).

For alternate configurations $\mathcal{A}_4$ and $\mathcal{A}_8$, the growth rate ω_i is independent of the nodal line location and the mode is degenerate, as a result of the remaining discrete rotational symmetry. Arrangement $\mathcal{A}_8$ leads to stable operation and the oscillations in configuration $\mathcal{A}_4$ correspond to mixed modes at a reduced amplitude level (see Appendix C).

Equation (4.31) highlights interesting features for configurations $\mathcal{C}_2$, $\mathcal{C}_4$, $\mathcal{C}_6$, $\mathcal{L}_2$, $\mathcal{L}_4$, $\mathcal{L}_6$ and $\mathcal{L}_8$. Theoretically, these configurations, for which the splitting strength is expected to take high values, present two distinct eigenvalues associated with two different growth rates and eigenfrequencies. The two resulting modes are standing and the associated nodal lines are perpendicular. Depending on the growth rate values, one mode can prevail and be effectively observed in practice. Power spectral densities of the pressure signals for these cases, reported in Appendix C, feature a single well-defined peak. A standing mode with a fixed nodal line is observed and the other analytically possible mode, with a nodal line perpendicular to the first mode, is not observed experimentally. Examining the mathematical properties of (4.31), two extrema appear for two perpendicular nodal line positions (it is worth stressing at this point that, in figure 15, although only two possible standing modes are predicted theoretically for these cases, the growth rate ω_i is evaluated for a range of nodal line positions θ_n to examine the change in shape of the function for these different staging patterns). For configurations $\mathcal{C}_2$, $\mathcal{C}_4$ and $\mathcal{C}_6$, (4.31) indicates that the nodal line leading to a maximum of the growth rate passes at equal distances from the S-injectors which is consistent with the experimental observations. For type $\mathcal{L}$ configurations, the corresponding nodal lines are aligned with the diameter joining the centres of the two groups of S-injectors placed on opposite sides of the annular chamber. Hence, of the two possible nodal line orientations for these non-degenerate cases, the nodal line leading to a maximum growth rate is selected and indeed observed experimentally. To finish, the difference between the maximum and minimum value of the growth rate increases with the number of S-injectors for these cases, and this can be interpreted as reflecting an increase in the value of the splitting strength.

4.4. *Growth rate calculations and estimation of the damping rate*

It is now instructive to consider the growth rates associated with different configurations and use their values to derive an estimate of the damping rate corresponding to instabilities coupled by the 1A1L mode.

The damping rate α plays a key role in thermoacoustic analysis but its value is generally not measured or quoted. A theoretical estimate is difficult to obtain because the processes that give rise to damping are not always easy to model. One possibility consists in using resonance techniques and measuring the quality factor of the system under stable operation. This only gives an effective damping rate α' that needs to be corrected for the flame influence (Paliès *et al.* 2011). A second approach relies on system identification

methods applied to simultaneous recordings of pressure and heat release rate fluctuations (Boujo *et al.* 2016). A third possibility consists in estimating the Rayleigh source term under self-sustained oscillations at a limit cycle (Durox *et al.* 2009; Vignat 2020). Starting from (4.11),

$$\frac{\mathrm{d}\langle E\rangle}{\mathrm{d}t} = \langle S\rangle - \langle D\rangle - \int_A \boldsymbol{F}\cdot\boldsymbol{n}\,\mathrm{d}A \tag{4.35}$$

and assuming steady self-sustained oscillations, the $\mathrm{d}\langle E\rangle/\mathrm{d}t$ term vanishes, and one gets

$$\langle D\rangle + \int_A \boldsymbol{F}\cdot\boldsymbol{n}\,\mathrm{d}A = \langle S\rangle. \tag{4.36}$$

Hence, under steady self-sustained oscillations, the source term is in equilibrium with the acoustic losses, which result from damping and outgoing acoustic energy fluxes. The source term $\langle S\rangle$ was evaluated by Durox *et al.* (2009) and Vignat (2020) through simultaneous photomultipliers and microphone recordings. It is shown by Vignat (2020) that the latter method and the approach based on system identification proposed by Boujo *et al.* (2016) yield comparable results in the case of instabilities coupled by a purely axial mode.

In this section, growth rates ω_i are calculated using the analytical framework presented in § 4.1 for configurations $\mathcal{C}_0$, $\mathcal{C}_2$, $\mathcal{C}_4$, $\mathcal{C}_6$, $\mathcal{C}_7$ and $\mathcal{C}_8$, and then for $\mathcal{L}_2$, $\mathcal{L}_4$, $\mathcal{L}_6$, $\mathcal{L}_8$, $\mathcal{L}_{10}$ and $\mathcal{L}_{12}$, and finally for $\mathcal{A}_4$ and $\mathcal{A}_8$. These results are then used to estimate the damping rate. For a given configuration, the growth rate can be determined for any combination of $|a|$ and $|b|$, and one can then see which combination provides the highest growth rate. In many situations, equal values of these amplitudes ($|a| = |b|$) yield the maximum value. This is consistent with the experimental observations, as these configurations give rise to standing modes. Equation (4.29) with $|a| = |b|$ will hence be used to determine the growth rates. The nodal line location is the one leading to the maximum value of the growth rate.

It is worth recalling that the growth rates obtained with the analytical expression are determined for low levels of modulation amplitude, since FDF data are only available for levels of relative velocity fluctuations around 10 % in the frequency range of interest (around 800 Hz). They hence correspond to linear growth rates. The values of the growth rate will change with the level of modulation amplitude, $\omega_i = \omega_i(v' = 0)g(v'/\bar{v})$, where g can be increasing or decreasing for intermediate values of $v'/\bar{v}$ and then becomes a decreasing function of $v'/\bar{v}$ at high amplitude levels.

Figure 16 shows the evolution of the growth rate as a function of the number of S-injectors for $\mathcal{C}$, $\mathcal{L}$ and $\mathcal{A}$ configurations. For the three types of configurations investigated, the calculated growth rate decreases with the number of S-injectors in the system, and for a fixed number of S-injectors, growth rates for type $\mathcal{C}$ and $\mathcal{A}$ staging patterns are lower than those found for $\mathcal{L}$ arrangements.

The calculated values of the growth rates enable to get an estimate of the damping rate of the system: stable and unstable points enable to identify upper and lower bounds of the damping rate. If a point is unstable, its growth rate is higher than the damping rate of the system. If a point is stable, its growth rate is lower than the damping rate of the system. Hence, the unstable point with the lowest growth rate constitutes the upper limit of the damping rate, and the stable point with the highest growth rate, the lower limit. To distinguish between stable and unstable points, the two criteria defined by Latour *et al.* (2023) will be used.

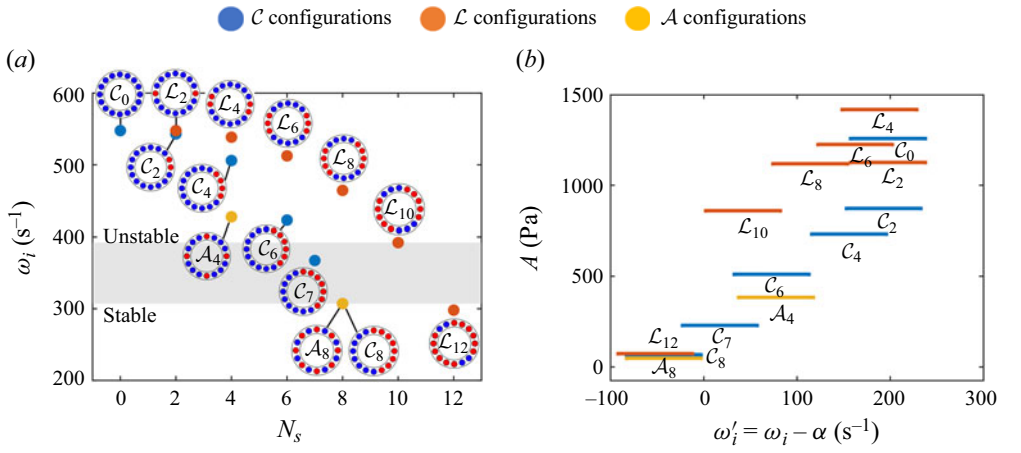

Figure 16. (*a*) Growth rates determined with the analytical model and (*b*) experimental instability amplitudes A as a function of the effective growth rate $\omega_i' = \omega_i - \alpha$ for configurations $\mathcal{C}_0$, $\mathcal{C}_2$, $\mathcal{C}_4$, $\mathcal{C}_6$, $\mathcal{C}_7$ and $\mathcal{C}_8$ (blue); $\mathcal{L}_2$, $\mathcal{L}_4$, $\mathcal{L}_6$, $\mathcal{L}_8$, $\mathcal{L}_{10}$ and $\mathcal{L}_{12}$ (orange); and $\mathcal{A}_4$ and $\mathcal{A}_8$ (yellow). The grey band appearing in panel (*a*) separates stable points from unstable points, providing an indication for the lower and upper values of the damping rate.

(i) The root mean square (r.m.s.) pressure is at least 3 times higher than a baseline level corresponding to the r.m.s. pressure level of noise under combustion and flow, measured for a stable operating point, which is typically 80 Pa.

(ii) The power spectral density exhibits a peak, $SPL^{m}_{\Delta f}$, that exceeds the maximum level measured in the baseline configuration, $SPL^{bl,m}_{\Delta f}$, by at least 25 dB: $SPL^{m}_{\Delta f} \geqslant SPL^{bl,m}_{\Delta f} + \Delta S$ (with $\Delta S = 25$ dB). This condition ensures that the signal is dominated by a well-defined frequency tone.

The upper and lower limits thus determined correspond to the grey band plotted in figure 16(*a*). Configuration $\mathcal{C}_7$, which is marginally unstable (the criterion for the r.m.s. pressure level is fulfilled, but not that for the power spectral density peak), is inside the grey band. One finds that the damping rate is between 310 and 390 s^{-1}. This value is consistent with that found by Vignat (2020), through source term evaluation from simultaneous photomultiplier and pressure measurements during self-sustained oscillations coupled by a longitudinal mode in the annular combustor MICCA-Spray.

One may ask whether the limit cycle amplitude can be linked in some way to the effective growth rate calculated in the linear range. Intuitively, one expects that high values of this rate will lead to high levels of oscillation. This possible link is examined in figure 16(*b*), where the instability amplitude A is plotted as a function of the effective growth rate $\omega_i' = \omega_i - \alpha$, determined analytically from lower and upper estimates of α (310 and 390 s^{-1}, corresponding to the grey band in figure 16*a*). One can see that configurations associated with high positive values of the effective growth rate correspond to high levels of limit cycle instability amplitude. Configurations associated with negative values of the effective growth rate correspond to stable operation in MICCA-Spray. It is also interesting to point out that for similar values of the growth rate, the level of pressure oscillations at limit cycle also depends on the type of configuration ($\mathcal{C}$, $\mathcal{L}$ or $\mathcal{A}$). This may be due to the fact that gain saturation (reflected by the g function in the expression $\omega_i = \omega_i(v' = 0)g(v'/\bar{v})$) depends on the configuration or that the damping rate changes with the configuration.

5. Conclusions

Different circumferential staging configurations are investigated experimentally in the laboratory-scale annular combustor MICCA-Spray by mixing two types of injectors, designated by U and S, featuring significantly different flame responses and correspondingly different flame describing functions. When all injectors are of the U-type, the system exhibits strong combustion instabilities coupled by the 1A1L mode and the azimuthal structure involves variable proportions of clockwise and counterclockwise waves. The nature of the mode is in that case of mixed type, with no preferred location for the pressure nodal line. When all injectors are of S-type, the regime of operation is stable. It is found that azimuthal arrangements in which the two types of injectors U and S are mixed notably influence the amplitude of oscillation and affect the modal nature. The changes in dynamics depend on the number and relative position of S-injectors. In a configuration where injectors of the same family are side-by-side, one observes that the oscillation amplitude is diminished as the number of S-injectors is augmented. When the S-injectors form two groups that are diametrically opposed, it is found that the coupling takes place through a standing 1A1L mode with a nodal line that is aligned with the median diameter connecting the two groups of S-injectors. Alternate configurations $\mathcal{A}$ involving four or eight S-injectors are shown to efficiently reduce the pressure oscillations in the annular system. An analytical framework relying on the acoustic energy balance equation is used to derive estimates of the growth rate, as a function of the injectors flame describing functions and of their circumferential location in the annular combustor. This general expression is used to explain many features observed experimentally. According to this expression, the growth rates corresponding to the spinning, mixed and standing modes are identically equal, when all the injectors are of the same type. It is next shown that when nodal line locking occurs for certain configurations of the S-injectors, the nodal line azimuthal orientation corresponds to a position that is such that the growth rate reaches its highest possible value. Another outcome of these experiments, in combination with the growth rate values, is the possibility to obtain an estimate of the damping rate for instabilities coupled by the 1A1L mode. In terms of practical implications, these findings indicate that azimuthal staging may be used to dampen thermoacoustic instabilities, but that the position of the injectors has to be carefully chosen since some arrangements dampen the instability, which is the case of 'side-by-side' arrangements or type $\mathcal{A}$ configurations, while others, in which the S-units occupy the two ends of a diameter, are much less effective or even lead to enhanced amplitudes of oscillation. Finally, the theoretical growth rate expressions derived in this article have more general value in that they give access to the stability rating of geometrically simple annular combustion systems.

Acknowledgements. The authors wish to thank Dr Y. Méry from Safran Aircraft Engines for suggesting to analyse the impact of azimuthal staging on the occurrence and level of instabilities. The authors also wish to thank the reviewers for their comments and suggestions.

Funding. This work is partially supported as part of France 2030 programme 'ANR-22-CE05-0022-02' FlySAFe project.

Declaration of interests. The authors report no conflict of interest.

Author ORCIDs.
V. Latour https://orcid.org/0009-0000-5293-7178.

Appendix A. Effect of head loss differences on the equivalence ratio

The pressure loss in an injection unit is typically expressed in terms of a bulk velocity U_b and a head loss coefficient as $\Delta p = \sigma(1/2)\rho U_b^2$. In the MICCA-Spray annular combustor, all the injectors have the same plenum for the air intake and the common fuel rail is pressurized at a high level, allowing a constant fuel flow rate in each injector. Let us consider a system with n_1 injectors of type 1 and n_2 injectors of type 2, with respective head loss coefficients σ_1 and σ_2. The bulk velocities in these two types of injectors are denoted U_1 and U_2. In what follows, one seeks to quantify the effects of the difference in head loss coefficient on the equivalence ratios at the different injectors.

The pressure loss through the two types of injectors must be the same so that

$$\Delta p = \sigma_1(1/2)\rho U_1^2 = \sigma_2(1/2)\rho U_2^2. \tag{A1}$$

This defines the ratio of the bulk velocities through the two types of units

$$\frac{U_1}{U_2} = \left(\frac{\sigma_2}{\sigma_1}\right)^{1/2}. \tag{A2}$$

Now, consider the total mass flow rate $\dot{m}$ in the system. If the head loss coefficients are all equal, the flow velocities in each injector are also equal:

$$\dot{m} = n\rho AU. \tag{A3}$$

If one now considers n_1 injectors of type 1 and n_2 injectors of 2, the total mass flow rate becomes

$$\dot{m} = n_1\rho AU_1 + n_2\rho AU_2. \tag{A4}$$

And replacing the left-hand side term by the expression in (A3), one has

$$n\rho AU = n_1\rho AU_1 + n_2\rho AU_2 \tag{A5}$$

and then using (A1), one finally obtains

$$U = \frac{n_1}{n}\left(\frac{\sigma_2}{\sigma_1}\right)^{1/2} U_2 + \frac{n_2}{n}U_2. \tag{A6}$$

Thus, the velocities through injectors 1 and 2 read

$$U_2 = U\frac{1}{1+\frac{n_1}{n}\left[\left(\frac{\sigma_2}{\sigma_1}\right)^{1/2}-1\right]}, \quad U_1 = U\frac{\left(\frac{\sigma_2}{\sigma_1}\right)^{1/2}}{1+\frac{n_1}{n}\left[\left(\frac{\sigma_2}{\sigma_1}\right)^{1/2}-1\right]}. \tag{A7a,b}$$

The relative differences in velocities in injectors 1 and 2 compared with the case where all the injectors are the same are

$$\frac{(U_2-U)}{U} = \frac{\frac{-n_1}{n}\left[\left(\frac{\sigma_2}{\sigma_1}\right)^{1/2}-1\right]}{1+\frac{n_1}{n}\left[\left(\frac{\sigma_2}{\sigma_1}\right)^{1/2}-1\right]}, \quad \frac{(U_1-U)}{U} = \frac{\frac{n_2}{n}\left[\left(\frac{\sigma_2}{\sigma_1}\right)^{1/2}-1\right]}{1+\frac{n_1}{n}\left[\left(\frac{\sigma_2}{\sigma_1}\right)^{1/2}-1\right]}. \tag{A8a,b}$$

n_S	1	2	3	4	5	6	7	8
$(\delta\phi/\phi)_U$	0.02	0.03	0.04	0.06	0.07	0.08	0.10	0.11
$(\delta\phi/\phi)_S$	−0.22	−0.20	−0.19	−0.17	−0.15	−0.14	−0.12	−0.11
ϕ_U	0.91	0.93	0.94	0.95	0.96	0.97	0.99	1.0
ϕ_S	0.70	0.72	0.73	0.75	0.76	0.78	0.79	0.80

Table 3. Effects of the number n_S of S injection units on the equivalence ratios of the U and S units.

The last two expressions indicate that if $\sigma_2 > \sigma_1$, then $U_2 < U$ and $U_1 > U$, and may now be used to quantify the impact in terms of global equivalence ratio. This quantity measures the mixture ratio with respect to its value under stoichiometric conditions

$$\phi = \frac{\dot{m}_f/\dot{m}_a}{(\dot{m}_f/\dot{m}_a)_{st}}. \tag{A9}$$

Since the mass flow rate of fuel is the same in all injectors, relative equivalence ratio perturbations resulting from the bulk velocity variations read

$$\frac{\delta\phi}{\phi} = -\frac{\delta\dot{m}_a}{\dot{m}_a} = -\frac{\delta U}{U}. \tag{A10}$$

Noting that injectors U and S are such that $\sigma_U > \sigma_S$, one immediately deduces that the operating point is shifted towards higher values of equivalence ratio for injectors U and towards lower values for injectors S. Table 3 gathers the equivalence ratio variations for different numbers of injectors S in the system.

One now seeks to quantify the effects of these equivalence ratio shifts on the dynamics of the flames formed by injectors U and S. When MICCA-Spray is equipped with $N = 16$ identical injectors, at the operating point chosen for this study, the global equivalence ratio is $\phi = 0.9$ and the thermal power $\mathcal{P}_{MICCA} = 118$ kW. FDFs were thus measured in SICCA-Spray for injectors S and U, at a fixed thermal power $\mathcal{P}_{SICCA} = \mathcal{P}_{MICCA}/N = 7.4$ kW, but for different equivalence ratios ($\phi = 0.8, 0.85$ and 0.9 for injector S and $\phi = 0.9, 0.95$ and 1.0 for injector U), to determine the effects of differences in equivalence ratio on flame dynamics. Measurements for equivalence ratios below $\phi = 0.8$ are not available because these operating points exceed the limits of the mass flow rate controllers.

The measured FDFs, plotted in figure 17, only feature slight differences between the nominal gain and phase curves obtained at $\phi = 0.9$ and those corresponding to the S-injector operating at $\phi = 0.8$ or 0.85. Similar observations also hold for injector U in the interval of equivalence ratios covered in the present experiments (from 0.9 to 1.0). Hence, the equivalence ratio variations resulting from the mixing of the different types of injectors only have a weak impact on the dynamics of the individual flames.

Appendix B. Determination of the effective impedance ζ

To evaluate the growth rate (4.29), one has to determine the effective impedance ζ that connects the pressure field to the velocity disturbances acting on the upstream side of the flame.

This impedance is here determined experimentally from the simultaneous recording of pressure and heat release fluctuations in a single experiment in which MICCA-Spray features self-sustained oscillations. A 'pressure-based' describing function, $\mathcal{F}_p$,

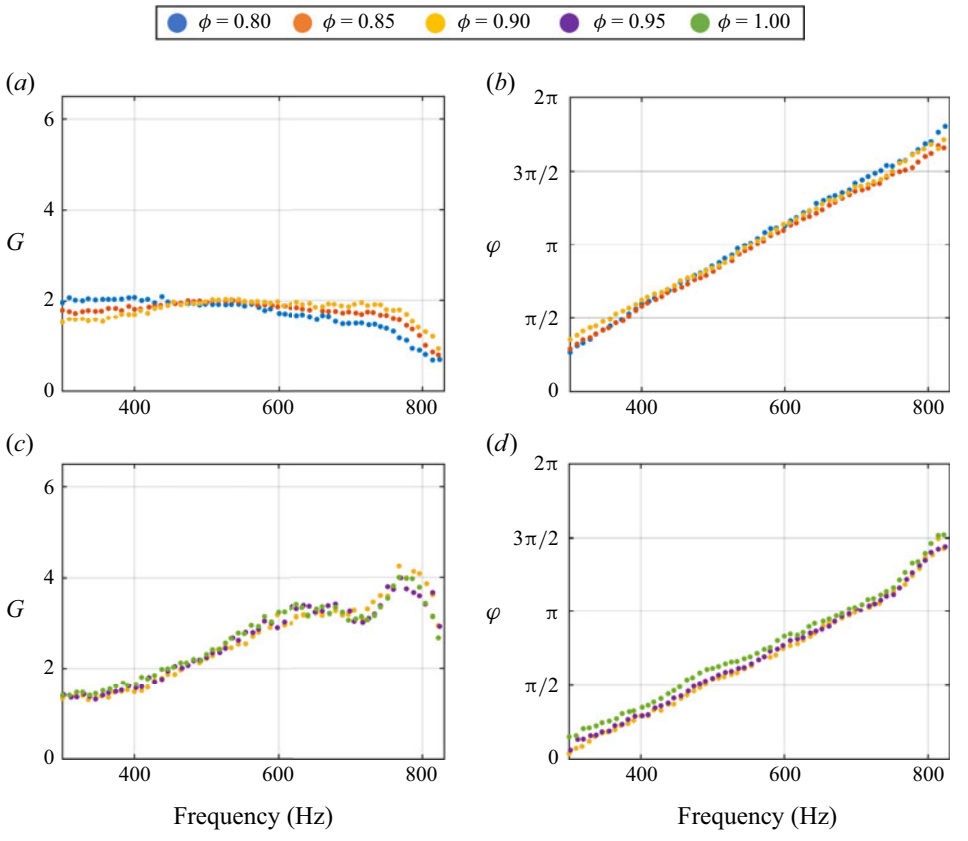

Figure 17. Effects of equivalence ratio on (*a*,*c*) FDF gain and (*b*,*d*) phase. Measurements were carried out in SICCA-Spray at a thermal power $\mathcal{P}_{SICCA} = 7.4$ kW. Only the curves corresponding to the lowest level of modulation amplitude are represented. (*a*,*b*) Injector *S* ($\phi = 0.8$, 0.85 and 0.9). (*c*,*d*) Injector *U* ($\phi = 0.9$, 0.95 and 1.0).

connecting the relative pressure and relative heat release rate fluctuations can be determined from these measurements for different flames in the annular combustor:

$$\mathcal{F}_p = \frac{\widetilde{\dot{Q}'}/\dot{Q}_0}{\tilde{p}/p_0}, \tag{B1}$$

where $\widetilde{\dot{Q}'}/\dot{Q}_0$ and $\tilde{p}/p_0$ correspond respectively to the relative heat release rate and pressure fluctuations, and $p_0 = 10^5$ Pa is a reference pressure.

One can then link the pressure-based FDF to the FDF, $\mathcal{F}$, and the impedance ζ using (4.18):

$$\mathcal{F}_p = \frac{\mathcal{F}}{\zeta}\frac{1}{\gamma M}. \tag{B2}$$

Finally, introducing $\mathcal{F}_p = G_p \mathrm{e}^{\mathrm{i}\varphi_p}$, one can express MG_ζ and φ_ζ as a function of the pressure-based FDF, and FDF gain and phase values, G_F and φ_F,

$$MG_\zeta = \frac{G_F}{G_p}\frac{1}{\gamma}, \quad \varphi_\zeta = \varphi_F - \varphi_p. \tag{B3a,b}$$

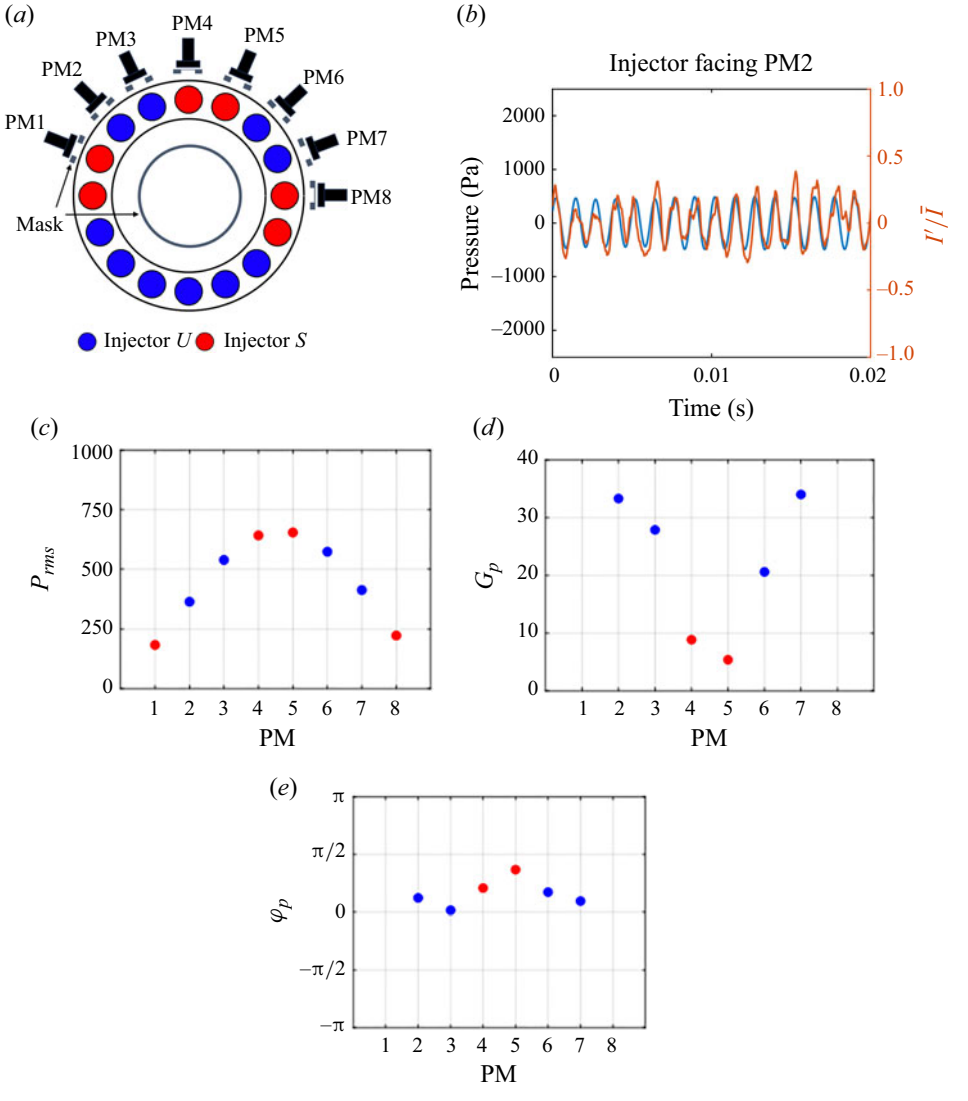

Figure 18. (*a*) MICCA-Spray set-up in configuration $\mathcal{L}_{4+2}$ for simultaneous photomultiplier (PM) and pressure recordings. (*b*) Simultaneous pressure and PM recordings at the injector facing PM2, used for the determination of MG_ζ and φ_ζ ('calibration injector'). (*c*) Pressure root mean square at the injectors facing PM1 to PM8, (*d*) pressure-based FDF gain and (*e*) phase at the injectors facing PM1 to PM8.

The FDF data being only available for small values of the relative velocity fluctuations, it is therefore necessary to use an experiment in which the level of oscillations is low and corresponds to the range that is covered by the available FDF dataset. This condition can be fulfilled by suitably choosing a configuration that leads to a low amplitude limit cycle.

The injectors arrangement (labelled '$\mathcal{L}_{4+2}$' and shown in figure 18, corresponding to configuration $\mathcal{L}_4$ to which two adjacent *S*-injectors are placed at the pressure anti-node) and the flame location in the annular system to be used for the determination of the impedance are chosen to ensure that pressure fluctuations levels are low or moderate so that the level of fluctuation is compatible with the available FDF data. Eight photomultipliers equipped with a 10 nm bandpass filter centred at 310 nm record the light intensity emitted

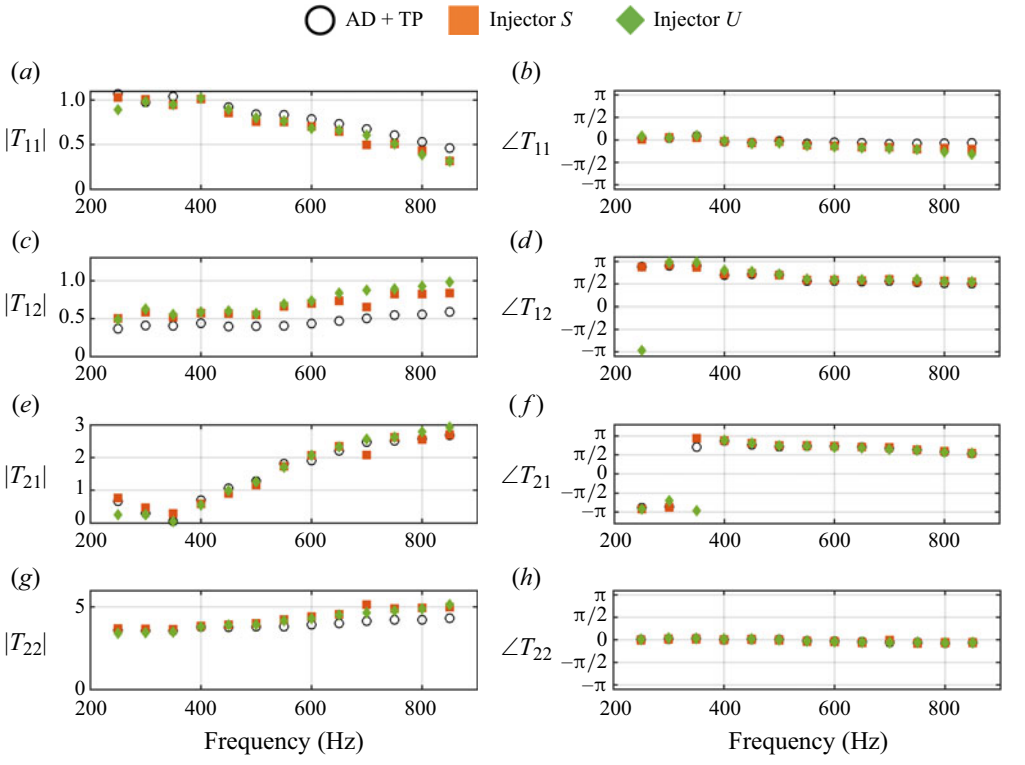

Figure 19. Transfer matrices of injectors U and S, and the injector without swirler, 'AD + TP' (for 'Air Distributor-Terminal Plate'), determined experimentally using the two-load method. The measurements were carried out in the presence of a bias flow and the resulting velocity at the injector outlet is $U_b = 12$ m s^{-1}.

by OH* for eight adjacent flames located on one half of the annulus. The experimental set-up, with the photomultipliers and microphones position, is displayed in figure 18. A mask, placed in front of each photomultiplier, acts as a spatial filter so that each sensor only records the light emitted by one flame. Another cylindrical mask, placed inside the inner cylindrical quartz, hides the flames in the background. For configuration $\mathcal{L}_{4+2}$, the mode is standing, and the measured r.m.s. pressure, P_{rms}, is reported for the injectors facing the eight photomultipliers in figure 18(*c*).

The gain and phase values of the obtained pressure-based FDFs are shown in figure 18. Only points presenting a coherence between the pressure and heat release rate signal above 0.9 are retained in this dataset (flames facing PM2 to PM7, the data corresponding to the flames facing PM1 and PM8 were removed). The flame used for the determination of MG_ζ is that facing PM2, designated as 'calibration injector' in figure 18, since in this position, the flame is submitted to a moderate level of pressure fluctuations and the signal-to-noise ratio remains good (see the pressure and PM recordings at the injector facing PM2 presented in figure 18*b*).

For the determination of MG_ζ and φ_ζ using (B3*a*,*b*), G_F and φ_F were evaluated at the instability frequency for configuration $\mathcal{L}_{4+2}$, $f = 800$ Hz. Additional experiments were carried out in SICCA-Spray to link velocity fluctuations to pressure fluctuations, to ensure that the range of pressure fluctuations for the FDF data is compatible with the level of pressure fluctuations measured in MICCA-Spray at the measurement point. One finally

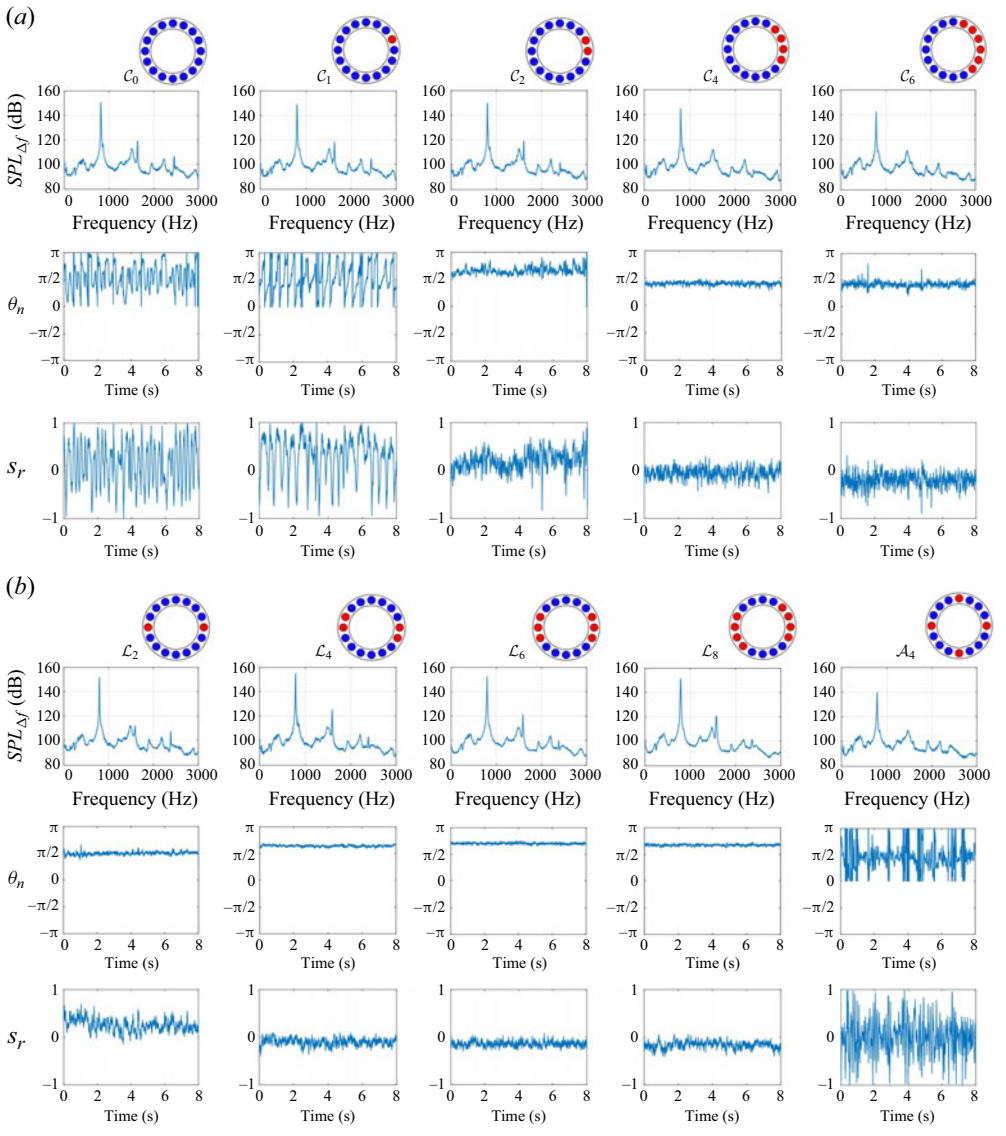

Figure 20. Pressure signal power spectral densities ($SPL_{\Delta f}$ in dB), spin ratio (s_r) and nodal line (θ_n) time series for configurations (*a*) $\mathcal{C}_0, \mathcal{C}_1, \mathcal{C}_2, \mathcal{C}_4$ and $\mathcal{C}_6$, and (*b*) $\mathcal{L}_2, \mathcal{L}_4, \mathcal{L}_6$ and $\mathcal{A}_4$. The origin and sign of the angles for the nodal line time series are defined in figure 13.

obtains $\varphi_\zeta = 1.2\pi$ and $MG_\zeta = 0.09$. These values are then used in the calculations in §§ 4.2 and 4.3 for all the arrangements investigated.

It is next shown that the impedance ζ can be assumed to be the same for the two types of injectors *U* and *S*. This assumption is supported by the transfer matrices obtained experimentally for injectors *U* and *S* using the two-load method (Munjal & Doige 1990). These matrices are displayed in figure 19. The transfer matrix coefficients for the injector without swirler, 'AD + TP' (Air Distributor-Terminal Plate) are also reported in figure 19 to determine the effect of the swirler on the transfer matrix of the injection units. Further details on the measurements can be found from Latour *et al.* (2024). Although these two injectors feature different pressure drop values, experimental results show that their

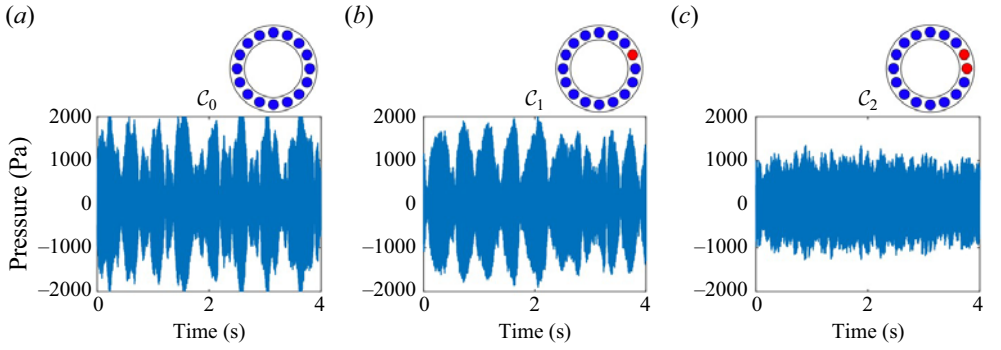

Figure 21. Pressure time series for configurations (*a*) $\mathcal{C}_0$, (*b*) $\mathcal{C}_1$ and (*c*) $\mathcal{C}_2$ showing a beating behaviour for arrangements $\mathcal{C}_0$ and $\mathcal{C}_1$.

transfer matrices are very close, and mainly determined by the air distributor and terminal plate, the swirler only having a small influence on the coefficients. Hence, the impedance can be considered to be the same for injectors U and S, $\zeta_S = \zeta_U$. One may then infer that the differences in flame dynamics observed between injectors S and U have their origin in differences in flame structures and their response to incident disturbances rather than in changes in the acoustic impedance at the flame.

Appendix C. Degenerate and non-degenerate mode features

The pressure signal power spectral densities (PSDs) along with the spin ratio and the nodal line time series are displayed in figure 20 for configurations $\mathcal{C}_0, \mathcal{C}_1, \mathcal{C}_2, \mathcal{C}_4, \mathcal{C}_6, \mathcal{L}_2, \mathcal{L}_4, \mathcal{L}_6, \mathcal{L}_8$ and $\mathcal{A}_4$ to complete the modal analysis of § 4.3. The origin and sign of the angles for the nodal line time series are defined in figure 13.

A single peak appears in the PSD of the pressure signal for these unstable configurations, indicating that, for the non-degenerate modes associated to staging patterns for which the splitting strength is expected to take high values ($\mathcal{C}_2, \mathcal{C}_4, \mathcal{C}_6, \mathcal{L}_2, \mathcal{L}_4, \mathcal{L}_6$ and $\mathcal{L}_8$), only one mode, shown to correspond to the maximum value of the growth rate (see § 4.3), is observed in practice.

The PSD for arrangement $\mathcal{C}_1$ features a single peak, but the associated pressure recordings exhibit a beating oscillation (see figure 21, where the pressure time series for configurations $\mathcal{C}_0, \mathcal{C}_1$ and $\mathcal{C}_2$ are reported), hinting that the splitting strength induced by symmetry breaking only leads to a small frequency difference between the two modes (smaller than the frequency resolution of the spectrum which is $\Delta f = 4$ Hz). This beating disappears in configuration $\mathcal{C}_2$.

To finish, the mode is expected to remain degenerate for case $\mathcal{C}_0$, and the power spectral densities of the pressure recordings feature a single peak. However, a beating behaviour is observed in the pressure signal (see figure 21*a*), which may possibly be linked to the slight break in symmetry due to the bulk swirling flow induced in the annular system, as discussed by Bauerheim *et al.* (2015). This hypothesis may be verified by estimating the frequency split resulting from the presence of a tangential mean flow in the annular chamber MICCA-Spray. The latter can be expressed as

$$\Delta f = 2 f_{11} \frac{v_\theta}{c} \tag{C1}$$

with v_θ the tangential velocity, f_{11} the eigenfrequency of the 1A1L mode, and c the speed of sound determined for a burnt gas temperature $T = 1500$ K. For the configuration at hand, one can estimate $v_\theta = 1.7$ m s^{-1}, leading to $\Delta f = 3.5$ Hz, which is indeed below the frequency resolution.

References

Aguilar, J.G., Dawson, J.R., Schuller, T., Durox, D., Prieur, K. & Candel, S. 2021 Locking of azimuthal modes by breaking the symmetry in annular combustors. *Combust. Flame* **234**, 111639.

Bauerheim, M., Cazalens, M. & Poinsot, T. 2015 A theoretical study of mean azimuthal flow and asymmetry effects on thermo-acoustic modes in annular combustors. *Proc. Combust. Inst.* **35** (3), 3219–3227.

Bauerheim, M., Ndiaye, A., Constantine, P., Moreau, S. & Nicoud, F. 2016 Symmetry breaking of azimuthal thermoacoustic modes: the UQ perspective. *J. Fluid Mech.* **789**, 534–566.

Bauerheim, M., Salas, P., Nicoud, F. & Poinsot, T. 2014 Symmetry breaking of azimuthal thermo-acoustic modes in annular cavities: a theoretical study. *J. Fluid Mech.* **760**, 431–465.

Bothien, M.R., Noiray, N. & Schuermans, B. 2015 Analysis of azimuthal thermo-acoustic modes in annular gas turbine combustion chambers. *Trans. ASME J. Engng Gas Turbines Power* **137** (6), 061505.

Boujo, E., Denisov, A., Schuermans, B. & Noiray, N. 2016 Quantifying acoustic damping using flame chemiluminescence. *J. Fluid Mech.* **808**, 245–257.

Bourgouin, J.-F., Durox, D., Moeck, J.P., Schuller, T. & Candel, S. 2013 Self-sustained instabilities in an annular combustor coupled by azimuthal and longitudinal acoustic modes. In *Proceedings of ASME Turbo Expo. 2013*. Paper GT2013-95010. ASME.

Campa, G. & Camporeale, S.M. 2014 Prediction of the thermoacoustic combustion instabilities in practical annular combustors. *Trans. ASME J. Engng Gas Turbines Power* **136** (9), 091504.

Candel, S. 2002 Combustion dynamics and control: progress and challenges. *Proc. Combust. Inst.* **29** (1), 1–28.

Dawson, J.R. & Worth, N.A. 2015 The effect of baffles on self-excited azimuthal modes in an annular combustor. *Proc. Combust. Inst.* **35** (3), 3283–3290.

Dowling, A.P. 1997 Nonlinear self-excited oscillations of a ducted flame. *J. Fluid Mech.* **346**, 271–290.

Durox, D., Prieur, K., Schuller, T. & Candel, S. 2015 Different flame patterns linked with swirling injector interactions in an annular combustor. In *Proceedings of ASME Turbo Expo. 2015*. Paper GT2015-42034. ASME.

Durox, D., Schuller, T. & Candel, S. 2002 Self-induced instability of a premixed jet flame impinging on a plate. *Proc. Combust. Inst.* **29** (1), 69–75.

Durox, D., Schuller, T., Noiray, N., Birbaud, A.L. & Candel, S. 2009 Rayleigh criterion and acoustic energy balance in unconfined self-sustained oscillating flames. *Combust. Flame* **156**, 106–119.

Evesque, S. & Polifke, W. 2002 Low-order acoustic modelling for annular combustors: validation and inclusion of modal coupling. In *Proceedings of ASME Turbo Expo. 2002*. Paper GT2002-30064. ASME.

Evesque, S., Polifke, W. & Pankiewitz, C. 2003 Spinning and azimuthally standing acoustic modes in annular combustors. *Proceedings of the 9th AA/CEAS Aeroacoustics Conference and Exhibit. AIAA Paper* 2003-3182.

Fanaca, D., Alemela, P., Ettner, F., Hirsch, C., Sattelmayer, T. & Schuermans, B. 2008 Determination and comparison of the dynamic characteristics of a perfectly premixed flame in both single and annular combustion chambers. In *Proceedings of ASME Turbo Expo. 2008*. Paper GT2008-50781. ASME.

Faure-Beaulieu, A. & Noiray, N. 2020 Symmetry breaking of azimuthal waves: slow-flow dynamics on the Bloch sphere. *Phys. Rev. Fluids* **5** (2), 023201.

Fischer, A., Hirsch, C. & Sattelmayer, T. 2006 Comparison of multi-microphone transfer matrix measurements with acoustic network models of swirl burners. *J. Sound Vib.* **298**, 73–83.

Ghirardo, G. & Bothien, M.R. 2018 Quaternion structure of azimuthal instabilities. *Phys. Rev. Fluids* **3** (11), 113202.

Ghirardo, G., Ćosić, B., Juniper, M.P. & Moeck, J.P. 2015 State-space realization of a describing function. *Nonlinear Dyn.* **82** (1), 9–28.

Ghirardo, G. & Juniper, M.P. 2013 Azimuthal instabilities in annular combustors: standing and spinning modes. *Proc. R. Soc. Lond.* A **469** (2157), 20130232.

Ghirardo, G., Nygård, H.T., Cuquel, A. & Worth, N.A. 2021 Symmetry breaking modelling for azimuthal combustion dynamics. *Proc. Combust. Inst.* **38** (4), 5953–5962.

HAN, X., LI, J. & MORGANS, A.S. 2015 Prediction of combustion instability limit cycle oscillations by combining flame describing function simulations with a thermoacoustic network model. *Combust. Flame* **162** (10), 3632–3647.

HUANG, Y. & YANG, V. 2005 Effect of swirl on combustion dynamics in a lean-premixed swirl-stabilized combustor. *Proc. Combust. Inst.* **30**, 1775–1782.

HUANG, Y. & YANG, V. 2009 Dynamics and stability of lean-premixed swirl-stabilized combustion. *Prog. Energy Combust. Sci.* **35** (4), 293–364.

HUMBERT, S.C., MOECK, J.P., ORCHINI, A. & PASCHEREIT, C.O. 2021 Effect of an azimuthal mean flow on the structure and stability of thermoacoustic modes in an annular combustor model with electroacoustic feedback. *Trans. ASME J. Engng Gas Turbines Power* **143** (6), 061026.

HUMBERT, S.C., MOECK, J.P., PASCHEREIT, C.O. & ORCHINI, A. 2023 Symmetry-breaking in thermoacoustics: theory and experimental validation on an annular system with electroacoustic feedback. *J. Sound Vib.* **548**, 117376.

INDLEKOFER, T., AHN, B., KWAH, Y.H., WISEMAN, S., MAZUR, M., DAWSON, J.R. & WORTH, N.A. 2021 The effect of hydrogen addition on the amplitude and harmonic response of azimuthal instabilities in a pressurized annular combustor. *Combust. Flame* **228**, 375–387.

INDLEKOFER, T., FAURE-BEAULIEU, A., DAWSON, J.R. & NOIRAY, N. 2022 Spontaneous and explicit symmetry breaking of thermoacoustic eigenmodes in imperfect annular geometries. *J. Fluid Mech.* **944**, A15.

KOMAREK, T. & POLIFKE, W. 2010 Impact of swirl fluctuations on the flame response of a perfectly premixed swirl burner. *Trans. ASME J. Engng Gas Turbines Power* **132** (6), 061503.

KOPITZ, J., HUBER, A., SATTELMAYER, T. & POLIFKE, W. 2005 Thermoacoustic stability analysis of an annular combustion chamber with acoustic low order modeling and validation against experiment. In *Proceedings of ASME Turbo Expo. 2005*. Paper GT2005-68797. ASME.

KREBS, W., FLOHR, P., PRADE, B. & HOFFMANN, S. 2002 Thermoacoustic stability chart for high-intensity gas turbine combustion systems. *Combust. Sci. Technol.* **174** (7), 99–128.

LATOUR, V., DUROX, D., RAJENDRAM SOUNDARARAJAN, P., RENAUD, A. & CANDEL, S. 2023 Effects of fuel composition on azimuthal combustion instabilities in an annular combustor equipped with spray injectors. In *Proceedings of ASME Turbo Expo. 2023*. Paper GT2023-101370. ASME.

LATOUR, V., RAJENDRAM SOUNDARARAJAN, P., DUROX, D., RENAUD, A. & CANDEL, S. 2024 Assessing transfer matrix models and measurements using acoustic energy conservation principles. *Trans. ASME J. Engng Gas Turbines Power* **146** (1), 011021.

MAZUR, M., NYGÅRD, H.T., DAWSON, J.R. & WORTH, N.A. 2019 Characteristics of self-excited spinning azimuthal modes in an annular combustor with turbulent premixed bluff-body flames. *Proc. Combust. Inst.* **37** (4), 5129–5136.

MENSAH, G.A., MAGRI, L., ORCHINI, A. & MOECK, J.P. 2019 Effects of asymmetry on thermoacoustic modes in annular combustors: a higher-order perturbation study. *Trans. ASME J. Engng Gas Turbines Power* **141** (4), 041030.

MOECK, J.P., PAUL, M. & PASCHEREIT, C.O. 2010 Thermoacoustic instabilities in an annular Rijke tube. In *Proceedings of ASME Turbo Expo. 2010*. Paper GT2010-23577. ASME.

MUNJAL, M.L. & DOIGE, A.G. 1990 Theory of a two source-location method for direct experimental evaluation of the four-pole parameters of an aeroacoustic element. *J. Sound Vib.* **141** (2), 323–333.

NOIRAY, N., BOTHIEN, M. & SCHUERMANS, B. 2011 Investigation of azimuthal staging concepts in annular gas turbines. *Combust. Theory Model.* **15** (5), 585–606.

NOIRAY, N., DUROX, D., SCHULLER, T. & CANDEL, S. 2008 A unified framework for nonlinear combustion instability analysis based on the flame describing function. *J. Fluid Mech.* **615**, 139–167.

NOIRAY, N. & SCHUERMANS, B. 2013 On the dynamic nature of azimuthal thermoacoustic modes in annular gas turbine combustion chambers. *Proc. R. Soc. Lond.* A **469** (2151), 20120535.

ORCHINI, A., ILLINGWORTH, S.J. & JUNIPER, M.P. 2015 Frequency domain and time domain analysis of thermoacoustic oscillations with wave-based acoustics. *J. Fluid Mech.* **775**, 387–414.

PALIÈS, P., DUROX, D., SCHULLER, T. & CANDEL, S. 2011 Nonlinear combustion instability analysis based on the flame describing function applied to turbulent premixed swirling flames. *Combust. Flame* **158** (10), 1980–1991.

PANKIEWITZ, C. & SATTELMAYER, T. 2003 Time domain simulation of combustion instabilities in annular combustors. *Trans. ASME J. Engng Gas Turbines Power* **125** (3), 677–685.

PARMENTIER, J.-F., SALAS, P., WOLF, P., STAFFELBACH, G., NICOUD, F. & POINSOT, T. 2012 A simple analytical model to study and control azimuthal instabilities in annular combustion chambers. *Combust. Flame* **159** (7), 2374–2387.

PATAT, C., BAILLOT, F., BLAISOT, J.-B. & DOMINGUES, E. 2021 Responses of lean swirling spray flames to acoustic pressure and transverse velocity perturbations. In *Proceedings of the Symposium on Thermoacoustics in Combustion: Industry meets Academia (SoTiC 2021), Munich*.

POINSOT, T. 2017 Prediction and control of combustion instabilities in real engines. *Proc. Combust. Inst.* **36** (1), 1–28.

PRIEUR, K., DUROX, D., SCHULLER, T. & CANDEL, S. 2017 A hysteresis phenomenon leading to spinning or standing azimuthal instabilities in an annular combustor. *Combust. Flame* **175**, 283–291.

RAJENDRAM SOUNDARARAJAN, P., DUROX, D., RENAUD, A. & CANDEL, S. 2022*a* Azimuthal instabililities of an annular combustor with different swirling injectors. *Trans. ASME J. Engng Gas Turbines Power* **144** (11), 111018.

RAJENDRAM SOUNDARARAJAN, P., DUROX, D., RENAUD, A., VIGNAT, G. & CANDEL, S. 2022*b* Swirler effects on combustion instabilities analyzed with measured FDFs, injector impedances and damping rates. *Combust. Flame* **238**, 011016.

RAJENDRAM SOUNDARARAJAN, P., VIGNAT, G., DUROX, D., RENAUD, A. & CANDEL, S. 2021 Effect of different fuels on combustion instabilities in an annular combustor. *Trans. ASME J. Engng Gas Turbines Power* **143** (3), 031007.

SCHUERMANS, B., GUETHE, F., PENNELL, D., GUYOT, D. & PASCHEREIT, C.O. 2010 Thermoacoustic modeling of a gas turbine using transfer functions measured under full engine pressure. *Trans. ASME J. Engng Gas Turbines Power* **132** (11), 111503.

SCHULLER, T., DUROX, D., PALIES, P & CANDEL, S. 2012 Acoustic decoupling of longitudinal modes in generic combustion systems. *Combust. Flame* **159**, 1921–1931.

SCHULLER, T., POINSOT, T. & CANDEL, S. 2020 Dynamics and control of premixed combustion systems based on flame transfer and describing functions. *J. Fluid Mech.* **894**, P1–P95.

STAFFELBACH, G., GICQUEL, L.Y.M., BOUDIER, G. & POINSOT, T. 2009 Large Eddy Simulation of self excited azimuthal modes in annular combustors. *Proc. Combust. Inst.* **32**, 2909–2916.

STOW, S.R. & DOWLING, A.P. 2003 Modelling of circumferential modal coupling due to Helmholtz resonators. In *Proceedings of ASME Turbo Expo. 2003*. Paper GT2003-38168. ASME.

VIGNAT, G. 2020 Injection and combustion dynamics in swirled spray flames and azimuthal coupling in annular combustors. PhD thesis, Université Paris-Saclay, France, pp. 238–248.

VIGNAT, G., DUROX, D., PRIEUR, K. & CANDEL, S. 2019 An experimental study into the effect of injector pressure loss on self-sustained combustion instabilities in a swirled spray burner. *Proc. Combust. Inst.* **37** (4), 5205–5213.

VIGNAT, G., RAJENDRAM SOUNDARARAJAN, P., DUROX, D., VIÉ, A., RENAUD, A. & CANDEL, S. 2021 A joint experimental and Large Eddy Simulation characterization of the liquid fuel spray in a swirl injector. *Trans. ASME J. Engng Gas Turbines Power* **143** (8), 081019.

WOLF, P., STAFFELBACH, G., GICQUEL, L., MÜLLER, J.-D. & POINSOT, T. 2012 Acoustic and Large Eddy Simulation studies of azimuthal modes in annular combustion chambers. *Combust. Flame* **159** (11), 3398–3413.

WORTH, N.A. & DAWSON, J.R. 2013 Modal dynamics of self-excited azimuthal instabilities in an annular combustion chamber. *Combust. Flame* **160** (11), 2476–2489.

WORTH, N.A. & DAWSON, J.R. 2017 Effect of equivalence ratio on the modal dynamics of azimuthal combustion instabilities. *Proc. Combust. Inst.* **36** (3), 3743–3751.